Physics of Fluids

Droplet impact on a heated porous plate above the Leidenfrost temperature: A lattice Boltzmann study

Accepted Manuscript: This article has been accepted for publication and undergone full peer review but has not been through the copyediting, typesetting, pagination, and proofreading process, which may lead to differences between this version and the Version of Record.

Cite as: Physics of Fluids (in press) (2022); https://doi.org/10.1063/5.0118079
Submitted: 03 August 2022 • Accepted: 29 August 2022 • Accepted Manuscript Online: 30 August 2022

Geng Wang, Linlin Fei, Timan Lei, et al.

View Online
Export Citation
CrossMark

Physics of Fluids
Special Topic: Hydrogen Flame and Detonation Physics
Submit Today!

Physics of Fluids (in press) (2022); https://doi.org/10.1063/5.0118079

(c) 2022 Author(s).

AIP Publishing

Droplet impact on a heated porous plate above the Leidenfrost temperature: A lattice Boltzmann study

Geng Wang[1] (王耿), Linlin Fei[2] (费林林), Timan Lei[1] (雷体蔓), Qian Wang[3] (王倩), Kai H. Luo[1*]（罗开红）

1 Department of Mechanical Engineering, University College London, Torrington Place, London WC1E 7JE, UK
2 Chair of Building Physics, Department of Mechanical and Process Engineering, ETH Zürich (Swiss Federal Institute of Technology in Zürich), Zürich 8092, Switzerland
3 School of Mechanical Engineering, Shanghai Jiao Tong University, Shanghai 200240, China

*Corresponding Author:
Email: k.luo@ucl.ac.uk

Abstract

In the past few decades, droplet impact on a heated plate above the Leidenfrost temperature has attracted immense research interest. The strong hydrophobicity caused by the Leidenfrost effect leads to the droplet bouncing from a flat plate at a given contact time predicted by the classical Rayleigh theory. Numerous investigations were conducted to break the theoretical Rayleigh's limit to reduce the interfacial contact time. Recently a droplet was observed to form a pancake shape and bounce as it impacted nanotube or micropost surfaces above the Leidenfrost temperature. This led to a significant reduction in droplet contact time. However, this unique bouncing phenomenon is still not fully understood, such as the influence of the plate configuration and the relationship between the droplet rebound time and evaporation mass loss. In this study, we carry out a numerical study of the droplet impact dynamics on a heated porous plate above the Leidenfrost temperature, using a multiphase thermal lattice Boltzmann model. Our model is constructed within the unified lattice Boltzmann method (ULBM) framework and is firstly validated based on theoretical and experimental results. Then, a comprehensive parametric study is performed to investigate the effects of the impact Weber number, the plate temperature and the plate configurations on the droplet bouncing dynamics. Results show that higher plate temperature, larger Weber number, and smaller pore intervals can accelerate the droplet rebound and promote the droplet pancake bouncing. We demonstrate that the occurrence of the pancake bouncing is attributed to the additional lift force provided by the vapour pressure due to the evaporation of liquid inside the pores. Moreover, the droplet maximum spreading time and maximum spreading factor can be described by a power law function of the impact Weber number. The droplet evaporation mass loss increases linearly with the impingement Weber number and the plate opening fractions. This study provides new insights into the Leidenfrost droplet impingement on porous plates, which may potentially facilitate the design of novel engineering surfaces and devices.

1. Introduction

Droplet impingement on a heated plate is ubiquitous in nature and the industry such as aviation, power generation and process engineering [1,2]. Recently, the rapid development of miniaturized electronic devices creates an urgent need for innovative cooling approaches, such as spray cooling, which requires optimized manipulation of droplet dynamics on a heated plate [3]. This demands detailed insights into the effects of the plate temperature, plate geometry and liquid properties on droplet impact dynamics and its evaporation over the heated plate [4–6]. According to the classical boiling heat transfer theory, the droplet experiences several heating regimes when the plate temperature is increased, for example, the nucleate boiling regime, the transition boiling regime and the film boiling regime [1,7]. Remarkably, in the film boiling regime, the plate temperature is above the Leidenfrost point and the droplet's lower surface evaporates rapidly. As a result, a thin vapour layer is generated between the liquid phase and the solid plate, impeding the contact of the droplet with the plate. The Leidenfrost droplet thus demonstrates similar dynamics as its impingement on superhydrophobic surfaces [4]. For example, it has been observed that a droplet rebounds after impacting a hot plate above the Leidenfrost temperature. On a flat plate, the contact time (t_c) of the droplet approximately follows Rayleigh’s theory, where $t_c/\tau\ = \pi/4$ ($\tau = ({D_0}^3 \rho_l/\sigma)^{0.5}$ is the inertia-capillarity time) [4,8–10]. Also, the vapour layer between the droplet and the heated plate prevents heat transfer and droplet evaporation, which minimizes the heat flux at the Leidenfrost point [1,7]. Considering that the solid-liquid interface contact time is critical to applications such as anti-icing, spray cooling and heat transfer, the study of droplet impingement dynamics on superhydrophobic surfaces [11,12] and heated surfaces [4] has attracted increasing interest in the past few decades.

Considerable efforts have been made to experimentally explore the Leidenfrost droplet dynamics. Recent advances can be generally divided into three families: (1) Understanding of the Leidenfrost droplet hydrodynamics. Lagubeau *et al.* [13] first observed self-propelled characteristics of the Leidenfrost droplet on a ratchet surface, which was attributed to the interaction of the vapour flow and asymmetric textures. In 2018, Bouillant *et al.* [14] found the Leidenfrost droplet also demonstrated self-propelled characteristics on a hot flat plate. More recently, an interesting self-bouncing mechanism was observed for a deposited Leidenfrost droplet on a hot surface [15]. (2) Controlling of the Leidenfrost point to benefit the heat transfer. Franck *et al.* [16] found that the Leidenfrost point could drop to room temperature as the ambient pressure decreased. Kwon *et al.* [17] and Kruse *et al.* [18] suggested that the Leidenfrost point was increased for any droplet in sparse hot texture surfaces. Daniel *et al.* [19] observed that the microholes array surfaces can decrease the Leidenfrost point. More recently, Jiang *et al.* [20] inhibited the Leidenfrost point to over 1000 °C by designing the steel pillar surfaces with an insulating membrane. (3) Reducing the droplet contact time to break the limitation of Rayleigh's theory. Liu *et al.* [21] observed an explosive pancake bounce as the Leidenfrost droplet impacts on a surface with micro-scale micropore or micropost arrays, which significantly decreased the droplet contact time. Similar explosive pancake bouncing and contact time decreasing phenomena were observed when the Leidenfrost droplet impinged on a surface with nanotubes [22,23]. Besides, the explosive bounce has been observed for a multicomponent [24] droplet or a contaminated droplet [25] impacting on a heated plate over the Leidenfrost temperature.

In addition to experimental studies, with the rapid development of computer technologies in recent decades, numerical methods are being increasingly adopted to study the Leidenfrost droplet dynamics. Compared with traditional experimental methods, numerical methods have the advantages of precise control of the physical parameters, convenience to obtain quantitative data and ease to change the experimental configurations. Some early studies used the volume of fluid (VOF) algorithm to simulate droplet impact on a flat surface above the Leidenfrost temperature [26–28]. However, it is still challenging to couple the traditional 'interface tracking' multiphase model with the phase change model. Some studies introduced a virtual vapour layer with a pressure-dependent model [26] or a one-dimensional model [27,28] to prevent direct contact of the droplet with the hot plate. More recently, Chakraborty *et al.* [29] developed a lubrication model to predict the fluid flow inside the vapour layer of Leidenfrost drops.

Nevertheless, the capture of the vapour layer in most previous numerical studies depends on artificial models. Alternatively, the Lattice Boltzmann method (LBM) provides a promising approach to model this complex phase change problem. Benefitting from its mesoscopic nature, the LBM is capable of incorporating realistic physical models of interfacial and phase change problems [30,31]. In the pseudopotential LBM, for example, a realistic equation of state (EOS) of the fluid can be introduced to deal with temperature-dependent phase change [32,33]. Remarkably, Li *et al.* [34] adopted a multiple-relaxation-time (MRT) pseudopotential LB model to simulate a Leidenfrost droplet self-propelled on ratchet surfaces. Both Xu *et al.* [35]

and Karami *et al.* [36] conducted systematic parametric studies for a two-dimensional (2D) droplet impacting a heat plate over the Leidenfrost point by using MRT LBM. Recently, Xu *et al.* [37] adopted a three-dimensional cascaded lattice Boltzmann method (CLBM) model proposed by Fei *et al.* [38] to simulate droplet impact on heated micropillar surfaces, which has reproduced the droplet impingement dynamics for a wide range of temperatures successfully.

Although many efforts have been devoted to exploring the Leidenfrost droplet dynamics on a flat plat, there have been no systematic investigations into Leidenfrost droplet impact on a heated porous plate with pore sizes ranging from nanometer to micrometer, let alone explanations for the complex physics at play. For this problem, the traditional experimental techniques face significant challenges in the precise control of the plate temperature, impact velocity and pore size [21]. It is also difficult to obtain quantitative data (such as the quality of evaporated liquid) and observe the fluid flow inside the pores. Therefore, it is critical to conduct a systematic numerical investigation of this problem. In this study, we adopt the unified lattice Boltzmann method (ULBM) with the entropic-multi-relaxation-time (KBC) collision operator combined with the phase-change pseudopotential multiphase model [39] to numerically study a droplet impacting on a heated porous plate above the Leidenfrost temperature. A comprehensive parametric study is conducted by changing the droplet impact Weber number (We), the plate temperature, and the plate configurations, which aims to gain further physical insights into mechanisms of this complex droplet dynamics through both qualitative and quantitative analyses. In Sec. 2, we provide a brief introduction to the LB models, followed by model validation against previous theoretical, numerical and experimental results. In Sec. 3, we conduct a detailed investigation into the influence of the impact Weber number, for various plate temperatures and geometries. Additionally, the effects of pore intervals are scrutinised. Finally, conclusions are drawn in Sec. 4.

2. Methodology

2.1 UCLBM (KBC) model for multiphase flow

In this section, we briefly introduce the LB method which is used in this study. The mesoscopic evolution equation of the ULBM in central moment space can be written as [39]:

$$f_i(\boldsymbol{x}+\boldsymbol{e}_i\Delta t, t+\Delta t) \equiv f_i^*(\boldsymbol{x},t) = \mathbf{M}^{-1}\mathbf{N}^{-1}(\mathbf{I}-\mathbf{S})\big|\tilde{T}_i\big\rangle + \mathbf{M}^{-1}\mathbf{N}^{-1}\mathbf{S}\big|\tilde{\mathrm{T}}_i^{eq}\big\rangle + \mathbf{M}^{-1}\mathbf{N}^{-1}(\mathbf{I}-\mathbf{S}/2)|C_i\rangle, \qquad (1.)$$

where i indexes the 19 discrete velocity set, f_i and f_i^* are the pre-collision and post-collision distribution functions, respectively. **I**, **M**, **N** and **S** are the unit matrix, transformation matrix, shift matrix and relaxation matrix, respectively. $|\tilde{T}_i\rangle$ is the moment set in the co-moving framework and superscript eq represents the equilibrium state. $|C_i\rangle$ is the discrete forcing term which includes the total force acting on the system. In this study, a consistent forcing scheme in central moment space proposed by Fei *et al.* [40] is adopted:

$$|C_i\rangle = [0, F_x, F_y, F_z, 0,0,0,0,0,0, F_x C_S^2, F_x C_S^2, F_y C_S^2, F_z C_S^2, F_y C_S^2, F_z C_S^2, 0,0,0]^{\mathrm{T}}. \tag{2.}$$

The explicit expressions of matrix $\mathbf{M}, \mathbf{N}, \mathbf{M}^{-1}, \mathbf{N}^{-1}$ as well as the moment sets $|\tilde{T}_i\rangle$ and $|\tilde{T}^{eq}\rangle$ are given in Ref. [39]. It has been comprehensively proven that the ULBM framework has the ease to incorporate improved LB schemes [41] and excellent portability across different lattice models [40,42]. The KBC entropic operator [43] is implemented by introducing the entropic stabilizer into the higher-order relaxation parameters, hence the relaxation matrix $\mathbf{S}$ can be written as:

$$\mathbf{S} = diag(0,1,1,1, s_v, s_v, s_v, s_v\gamma, s_v, s_v, s_v\gamma, s_v\gamma, s_v\gamma, s_v\gamma, s_v\gamma, s_v\gamma, s_v\gamma, s_v\gamma, s_v\gamma), \tag{3.}$$

where $1/s_v = \nu/(C_S^2\Delta t) + 0.5$ depends on the liquid kinematic viscosity. The entropic stabilizer γ is calculated by:

$$\gamma = \frac{1}{s_v} - \left(1 - \frac{1}{s_v}\right)\sum_i \frac{\Delta s_i \Delta h_i}{f_i^{eq}} \Big/ \sum_i \frac{\Delta h_i \Delta h_i}{f_i^{eq}}, \tag{4.}$$

where s_i and h_i are the shear part and high order part of the distribution function, respectively. $\Delta s_i = s_i - s_i^{eq}$ and $\Delta h_i = h_i - h_i^{eq}$ are the deviations. The ULBM with the KBC operator has been shown to dramatically reduce spurious velocities [39]. More details about the ULBM (KBC) model can be found in Refs. [39,41].

For the multiphase flow simulation, the combined pseudopotential model [44] is employed to describe the interaction force among different phases, which is:

$$\boldsymbol{F_{int}} = -0.5AG\sum_i w(|\boldsymbol{e}_i|^2)\psi^2(\boldsymbol{x}+\boldsymbol{e}_i)\boldsymbol{e}_i - (1-A)G\psi(\boldsymbol{x})\sum_i w(|\boldsymbol{e}_i|^2)\psi(\boldsymbol{x}+\boldsymbol{e}_i)\boldsymbol{e}_i, \tag{5.}$$

where A is a tunable parameter which can be used to adjust the thermodynamic consistency, $G = -1$ is the interaction strength, $w(|\boldsymbol{e_i}|^2)$ are the weights for the D3Q19 lattice model. ψ is the square-root-form pseudopotential [45]:

$$\psi = \sqrt{\frac{2(P_{EOS} - \rho c_s^2)}{Gc^2}}, \tag{6.}$$

where $c = 1$ is the lattice constant, $c_s^2 = 1/3$ is the lattice sound speed and P_{EOS} is the pressure calculated by the equation of state (EOS). In this work, in order to simulate the multiphase flow with phase change phenomena, we use the Peng–Robinson EOS, which can be written as:

$$P_{EOS}=\frac{\rho RT}{1-b\rho}-\frac{a\varphi(T)\rho^2}{1+2b\rho-b^2\rho^2}, \tag{7.}$$

where $a=0.4572R^2T_c^2/P_c$, $b=0.0778RT_c/P_c$, and $\varphi(T)=\left[1+(0.37464+1.54226\omega-0.26992\omega^2)(1-\sqrt{T/T_c})\right]^2$, P_c and T_c stand for the critical pressure and critical temperature, respectively. In the following simulations, without specifying, we set R = 1, ω = 0.344, a = 1/76 and b = 2/21, with the corresponding $T_c=0.02351$ and $P_c=0.0192$.

In addition, when simulating the Leidenfrost droplet impingement, the gas phase and liquid phase are driven by the buoyancy force:

$$\boldsymbol{F_b}=-(\rho-\rho_{avg})g\boldsymbol{j}, \tag{8.}$$

where ρ_{avg} is the average density of the liquid and vapour phases. The total force acting on the fluid is $\boldsymbol{F}=\boldsymbol{F_b}+\boldsymbol{F_{int}}$. The improved virtual-density scheme proposed by Li *et al.* [46] is employed to treat the interaction between the solid phase and liquid phase. The virtual density of the bounded layer in the solid phase can be described as:

$$\rho_w(\boldsymbol{x})=\frac{\sum_i w(|\boldsymbol{e_i}|^2)\rho(\boldsymbol{x}+\boldsymbol{e_i}\Delta t)s(\boldsymbol{x}+\boldsymbol{e_i}\Delta t)}{\sum_i w(|\boldsymbol{e_i}|^2)s(\boldsymbol{x}+\boldsymbol{e_i}\Delta t)}, \tag{9.}$$

where $s(\boldsymbol{x})$ is an indicator function which is equal to 0 for the solid phase and 1 for the fluid phase, respectively. Based on this setup, the interaction force between the solid phase and liquid phase can be calculated by Eq. (5), and the droplet static contact angle under the isothermal condition equals 90°. It should be mentioned that the above multiphase ULBM (KBC) model has been verified by existing experiments of droplet dynamics. More details can be found in our recent work [37].

Inspired by Li et al. [47], the temperature field for the liquid-vapour phase-change can be written as:

$$\frac{\partial T}{\partial t}=-\boldsymbol{u}\cdot\nabla T+\frac{1}{\rho c_v}(\lambda\nabla^2T+\nabla\lambda\cdot\nabla T)-\frac{T}{\rho c_v}\left(\frac{\partial P_{EOS}}{\partial T}\right)_\rho\nabla\cdot\mathbf{u}, \tag{10.}$$

where λ is the thermal conductivity and c_v is the specific heat capacity at constant volume. Following the work of Fei *et al.* [38], we use the finite difference method to solve the above temperature equation, and the time discretization is realized using the fourth-order Runge–Kutta scheme:

$$T^{\mathrm{t}+\Delta\mathrm{t}}=T^{\mathrm{t}}+\frac{\Delta t}{6}(h_1+2h_2+2h_3+h_4),$$

$$h_1=K(T^t),h_2=K\left(T^t+\frac{\Delta t}{2}h_1\right),h_3=K\left(T^t+\frac{\Delta t}{2}h_2\right),h_4=K(T^t+\Delta th_3), \tag{11.}$$

where $K(T)$ denotes the right hand of Eq. (10). The coupling of the temperature field and the liquid-vapour phase change is achieved through the EOS of the fluid (Eq. (7)). It is worth mentioning that the phase change multiphase model presented above has been incorporated into the ULBM (with cascaded lattice Boltzmann model) to simulate the three-dimensional pool boiling [38,41].

2.2 Verification of the multiphase thermal LB model

We first validate the thermodynamic consistency of the adopted multiphase model. We simulate a flat surface and change the system temperature from $0.5T_c$ to $0.9T_c$, keeping the turntable parameter A in Eq. (5) at -0.88. We compare the simulated coexistence densities of the gas phase and the vapour phase with the Maxwell equal-area rules. As presented in Figure 1, the simulated coexistence densities (triangle symbols) coincide with the Maxwell construction results (lines) for a wide range of temperatures and density ratios (up to 6700), which proves the good thermodynamic consistency of our numerical model. We also simulate a static droplet with the initial radius $R_0 = 50$ lattices located at the centre of a $4R_0 \times 4R_0 \times 4R_0$ box, with the periodic boundaries in all directions. The density profile can be described by the following function:

$$\rho(r) = \frac{\rho_l + \rho_g}{2} + \frac{\rho_l - \rho_g}{2} \tanh\left[\frac{2(r - R_0)}{W}\right], \tag{12.}$$

where $W = 4$ is the approximate interface thickness by adopting the introduced setup in Sec. 2.1, and r represents the distance to the droplet centre. ρ_l and ρ_g are coexistence densities in the gas phase and vapour phase, respectively. A is set as -0.84 and the system temperatures are varied from $0.68T_c$ to $0.88T_c$, while all the other parameters kept the same. As indicated in the figure, the simulated coexistence densities for the droplet test (circle symbols) are also consistent with the maxwell construction results. Importantly, the maximum spurious velocities are lower than 0.0025 for all simulations due to the use of the ULBM (KBC) collision operator.

Further verification of the model considering the temperature field is conducted by simulating the evaporation of a single droplet. We simulate a liquid cylinder (equivalent to a 2D droplet) with an initial diameter $D_0 = 70$, evaporating in a temperature gradient. The simulation domain is set as $200 \times 200 \times 1$ with periodic boundaries in all directions. To compare with the results in Ref. [38], we set the temperature of the liquid phase as $0.86T_c$ and the surrounding vapour temperature as T_c, with $a = 2/49$ and $b = 2/21$ in the EOS. The kinematic viscosities and the specific heat capacities of the liquid phase and the gas phase are set as the same, e.g., $c_{v\_l} = c_{v\_g} = 6$, $\nu_l = \nu_g = 0.1$.

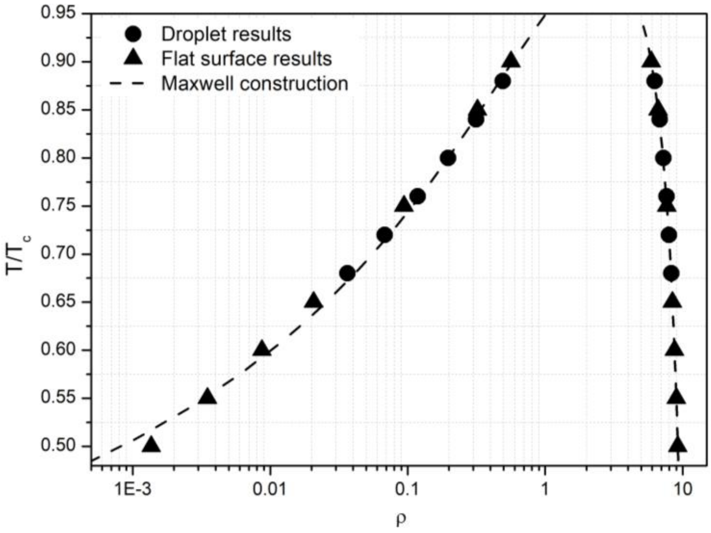

Figure 1. Comparison of the simulated coexistence densities (symbols) and the maxwell construction law (lines) for different reduced temperatures.

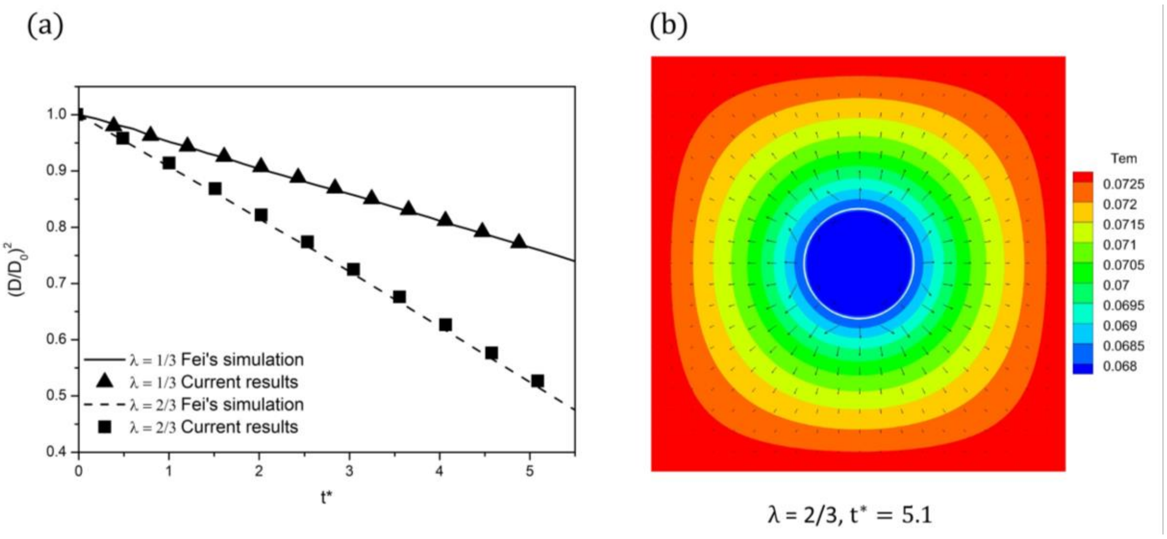

Figure 2. (a) Comparison of the evolution of (D/D_0)^2 for current simulation results (solid symbols) and previous simulation results(lines), for two different thermal conductivities, $\lambda_l = \lambda_g = 1/3$ and $\lambda_l = \lambda_g = 2/3$. (b) The temperature distribution and velocity vectors around the evaporating droplet (white profile).

The results of the current study (symbols) are compared with the previous simulation results (lines) [38] and D^2 law. To this end, the results are plotted as a $(D/D_0)^2$ versus t^* in Figure 2(a), where the non-dimensional time $t^* = T\nu_g/D_0^2$. As shown in the figure, our simulation results are in exact agreement with the previous simulation results for two different thermal conductivities, $\lambda_l = \lambda_g = 1/3$ and $\lambda_l = \lambda_g = 2/3$. Also, the temperature distribution and velocity vectors around the evaporating droplet are shown in Figure 2(b), demonstrating that the liquid phase evaporation is driven by the temperature gradient. The quantitative and qualitative results prove the accuracy of the model implementation for thermal multiphase flows.

2.3 Validation via Leidenfrost droplet impact on a flat plate.

Model validation is conducted via simulating droplet impact on a heated plate above the Leidenfrost temperature. In the following simulations, unless otherwise stated, the initial droplet radius is set as $R_0 = 50$. The liquid and vapour saturated temperature (T_s) is kept as $0.8T_c$, which leads to the corresponding coexistence densities at $\rho_l = 7.2$ and $\rho_l = 0.197$. By using this setup, the measured surface tension (σ) is 0.11235. According to Ref. [38], the latent heat (h_{fg}) of the droplet is calculated by:

$$h_{fg} = h_g - h_l = \int_{\rho_g}^{\rho_l} \frac{1}{\rho^2}\left[T\left(\frac{\partial P_{EOS}}{\partial T}\right)_\rho - P_{EOS}\right] d\rho + \frac{P_{EOS}}{\rho_g} - \frac{P_{EOS}}{\rho_l}, \tag{13.}$$

where h_g and h_l are the enthalpy values of the gas and liquid phases, respectively. Substituting the Peng-Robinson EOS in Sec. 2.1 into Eq. (13), the corresponding h_{fg} equals to 0.1416. Besides, we set the liquid kinematic viscosity (v_l) as 0.007 so that the Ohnesorge number is $Oh = (\rho_l v_l)/\sqrt{D_0 \rho_l \sigma} = 0.0056 < 0.01$, which implies the influence of the viscous force can be ignored compared with the inertial force and surface tension [48]. The kinematic viscosity ratio v_g/v_l between the gas phase and liquid phase is set as 20, which is comparable to the realistic condition.

To get an accurate prediction of the heat transfer and phase change process, we set the Prandtl number (the ratio of the momentum diffusivity to the thermal diffusivity) of the liquid phase ($Pr_l = v_l \rho_l c_{v_l}/\lambda_l$), Prandtl number of the gas phase ($Pr_g = v_g \rho_g c_{v_g}/\lambda_g$), and Jacob number $Ja = c_{v_l}(T_h - T_s)/h_{fg}$ (the ratio of the sensible heat to the latent heat during the phase change) comparable to the realistic conditions, with the thermal properties of the liquid and vapour phases referring to the values of the saturated state. Besides, the Weber number ($We = D_0 \rho_l U^2/\sigma$, representing the ratio of the inertial force to the capillary force, where U is the droplet initial velocity) and Bond number ($Bo = \rho_l g D_0^2/\sigma$, standing for the gravity compared to the surface tension, which is usually used to evaluate the influence of gravity) are also chosen to represent the experimental conditions. Based on the above setup, the corresponding fluid properties (e.g., c_v and λ) and operating parameters (e.g., U and g) in the lattice unit can be determined. For the following cases, we set $c_{v_l} = 7.4$, $c_{v_g} = 3.4$, $\lambda_l = 0.25$, $\lambda_g = 0.1$, which leads to $Pr_g = 0.94$ and $Pr_l = 1.49$, respectively. Remarkably, the following interpolation form is used to calculate the fluid properties at the liquid-gas interface:

$$X = X_g + (X_l - X_g)\frac{\rho - \rho_g}{\rho_l - \rho_g}, \tag{14.}$$

where X stands for the corresponding fluid properties.

It is worth mentioning that the conversion of a variable Γ from lattice (with subscript l) to physical units (with subscript p) is based on the characteristic variable (Γ_m), which can be written as $\Gamma_p = (\Gamma_{m,p}/\Gamma_{m,l})\Gamma_l$. For example, we choose the droplet diameter D_0 as the characteristic length, thus the physical length can be calculated by $L_p = (D_{0,p}/D_{0,l})L_l$. Regarding the calculation of the droplet initial velocity in lattice unit (U_l), it is based on the dimensionless Weber number, e.g., $U_l = \sqrt{\sigma We/\rho_l D_{0,l}}$. Additionally, the conversion from the simulation step (t_l) into the physical time (t_p) is based on the dimensionless time, where $t_p U_p/D_{0,p} = t_l U_l/D_{0,l}$.

Table 1. Experiment configurations and our simulation setups for the validation cases.

	Experiment conditions					**Simulation parameters**				
Case	Pr_g	Pr_l	Ja	We	Bo	Pr_g	Pr_l	Ja	We	Bo
1	0.76	1.57	0.48	2.1	0.18	0.94	1.49	0.53	2.1	0.14
2	0.76	1.57	0.51	16.3	0.23	0.94	1.49	0.61	16.0	0.19
3	0.76	1.57	0.34	22.8	0.18	0.94	1.49	0.50	21.6	0.16

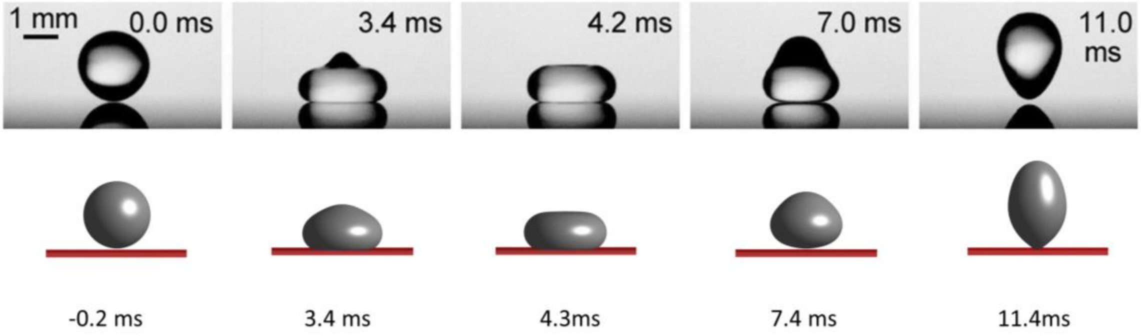

Figure 3. Experiment snapshots (top column) and simulation results (bottom column) of a droplet impacting an overheated flat plate with *We* = 2.1, *Ja* = 0.53.

Similar to Refs. [36,37], when simulating the Leidenfrost droplet impingement, the top wall of the simulation domain is set as the outflow boundary. The solid phase and bottom wall are set as the non-slip boundaries with the constant temperature T_h. The side walls of the simulation domain are set as the periodic boundaries. As pointed in Ref. [6], for most cases of droplet impact on a high temperature plate, the contact temperature between the droplet and the plate reaches the wall temperature immediately after the initial droplet contact. Consequently, we set the temperature of the fluid at the first layer near the solid wall as the wall temperature (T_h). Three cases with different impacting velocities and plate temperatures are simulated, and the experiment conditions and simulation setups of the corresponding cases are shown in Table 1.

The first case is to simulate the experiment in Ref. [49], where a water droplet with the initial diameter (D_0) of 2.05 mm impacts on a 385°C plate with a velocity $U = 0.24$ m/s. The simulation results for Case 1 are shown in Figure 3 (bottom column). It can be seen that after the droplet impacts the heated plate, it spreads in the horizontal direction. A very thin vapour film can be observed at the bottom of the droplet, which is generated by the evaporation of the contact liquid. Then, during the recoiling stage of the droplet, the levitated droplet re-contacted with the bottom wall. Finally, the droplet completely rebounds off from the plate, owing to the strong hydrophobic characteristics caused by the Leidenfrost effect. It can be observed that the simulation results agreed well with the experiment snapshots (top column) qualitatively.

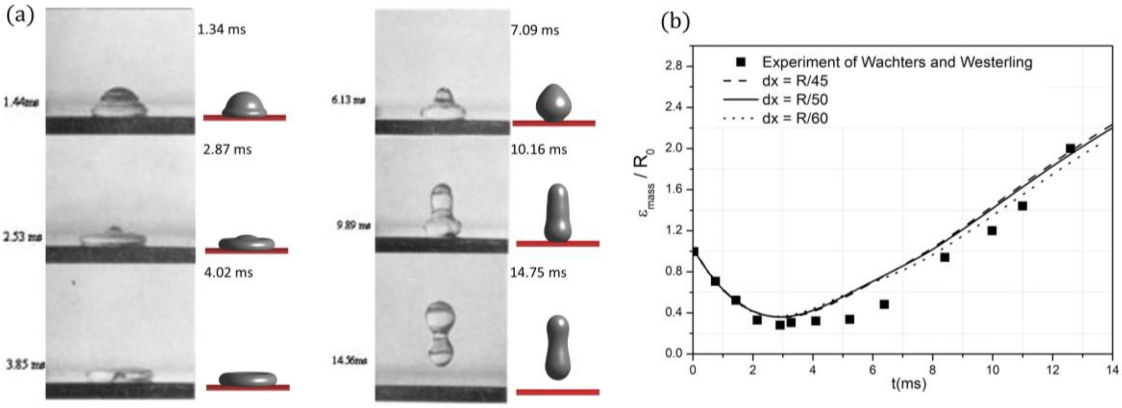

Figure 4. (a) A qualitative comparison of simulation results (right column) and experiment snapshots (left column) of droplet impact on a heated plate with *We* =16, *Ja* = 0.61. (b) Transient evolution of the height of the dimensionless droplet gravity centre (ε_{mass}/R_0), the lines represent the simulation results with various mesh resolutions and the symbols indicate the experiment results in Ref. [26].

We then simulate Leidenfrost droplet impact on an overheated plate with a higher Weber number (case 2 in Table 1). In the original experiment by Wachters and Westerling [50], the temperature of the hot plate is 400 °C, where the corresponding Jacob number *Ja* = 0.51. The droplet diameter is 2.3 mm and the impacting velocity is 0.63 m/s, leading to Weber number *We* = 15.7. The comparison of results is shown in Figure 4(a), and a qualitative agreement between the simulation and experimental results is achieved. Similar to Ref. [26], we quantitatively compare the evolution of droplet gravity central height (ε_{mass}) with the experimental data. In our simulation, the height of the droplet gravity centre is calculated by:

$$\varepsilon_{mass} = \frac{\sum_{\rho>\rho_{avg}} \rho(\boldsymbol{x})h(\boldsymbol{x})}{\sum_{\rho>\rho_{avg}} \rho(\boldsymbol{x})}, \tag{15.}$$

where $h(\boldsymbol{x})$ is the height of each cell and $\rho(\boldsymbol{x})$ represents the density of the cell. As indicated in Figure 4(b), after the droplet touches the plate, owing to the deformation of the droplet, ε_{mass} decreases from the centre of the sphere (R_0). After ε_{mass} reaches the minimum value during the spreading stage, it increases due to the droplet recoiling and rebound. The simulation results are in line with previous experimental data [50]. Additionally, we conduct a mesh independency study by increasing the mesh resolution to dx = $R_0/60$ or decreasing to dx = $R_0/45$. As shown in Figure 4(b), the evolution processes of ε_{mass} for all cases are consistent, which support the conclusion that the current mesh resolution (dx = $R_0/50$) is sufficiently fine for simulation.

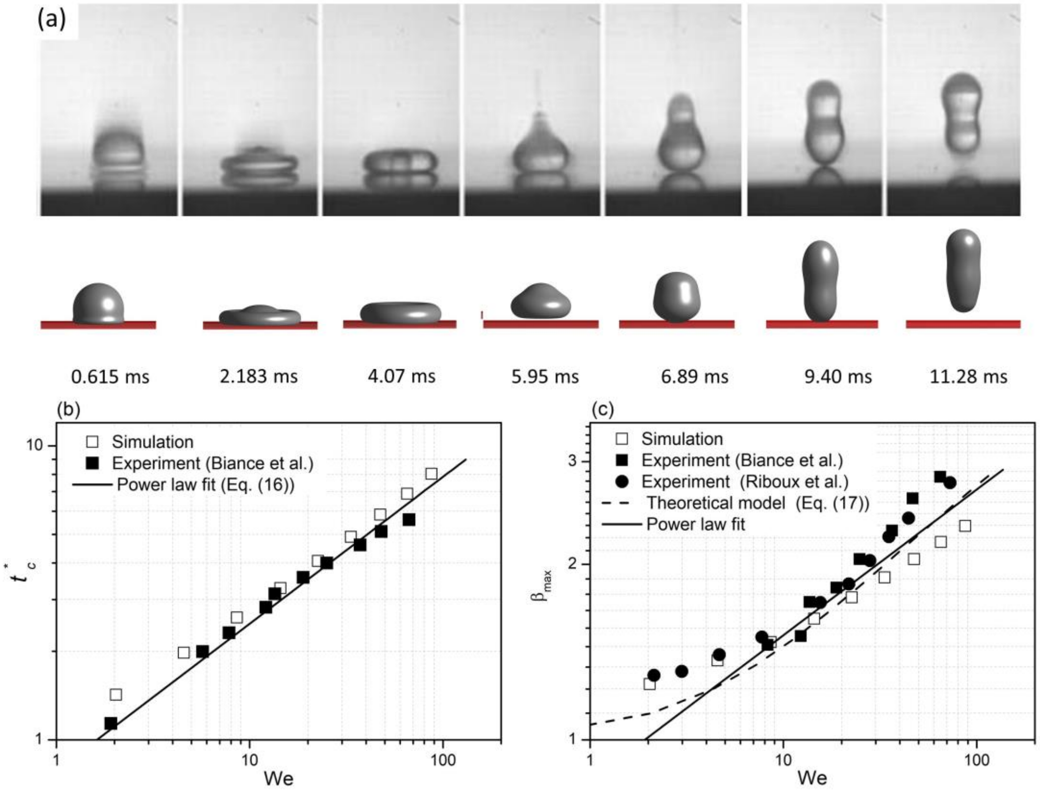

Figure 5. (a) Comparison of the experimental snapshots (top column) and simulation results (bottom column) of droplet impact on a heated plate at *We* = 21.5, *Ja* = 0.5. (b) The normalized

droplet contact time (t_c^*) as a function of Weber number, the simulation results (solid square symbols) are compared with the power law fitting equation (Eq. (16), solid line in the figure) and experiment results (hollow square symbols). (c) Comparison of the simulated droplet maximum spreading factors (β_{max}, hollow square symbols) with experiment results (solid symbols), experimental power law fitting equation (solid line) and theoretical prediction equation (dashed line).

The last validation is based on the experiment conducted by Biance *et al.* [51], corresponding to the experimental configurations and the simulation setup of case 3 in Table 1. The comparison in Figure 5(a) is for a water droplet ($R_0 = 1$ mm) impacting a 300 ℃ flat plate with an initial velocity at 0.8 m/s. As presented in the figure, our simulation results are generally consistent with the experiment results. Some deviations between the simulation and experimental snapshots can be found before the droplet bouncing, possibly because temperature-independent thermal properties are used in the current simulation. Besides, the constant contact temperature in our simulation may overestimate the evaporation rate of the droplet. Compared with the realistic situation, this setting could lead to a thicker vapour film between the droplet and the heated plate. Nevertheless, the current LBM model still provides a reliable prediction for the Leidenfrost droplet impingement, notably the thin vapour film between the droplet and hot plate, as well as the droplet bouncing owing to the Leidenfrost effect.

We then extend the simulation in Figure 5(a) to a wider range of impact Weber numbers by increasing the droplet initial velocity, with all the other setups kept the same. We qualitatively compare the normalized droplet contact time (t_c^*) and maximum spreading factor ($\beta_{\max}$) with the experimental data [51] and theoretical predictions. Figure 5(b) indicates the droplet contact time under various Weber numbers. In the figure, the droplet contact time is normalized by $t_c^* = Ut_c/D_0$. In previous literature [26,52,53], the theoretical contact time of the Leidenfrost droplet is approximately predicted by Rayleigh's theory [8], $t_c/\tau = \pi/4$, where $\tau = ({D_0}^3\rho_l/\sigma)^{0.5}$ is the inertia-capillarity time. Thus, the normalized droplet contact time can be re-written as:

$$t_c^* = \frac{t_c U}{D_0} = \frac{\pi}{4}\frac{U}{D_0}\sqrt{\frac{{D_0}^3\rho_l}{\sigma}} = \frac{\pi}{4}\sqrt{\mathrm{We}}. \qquad (16.)$$

We plot Eq. (16) as a solid line in Figure 5(b). As shown in the figure, our simulation results are in excellent agreement with the experimental data [51] and theoretical results, for a wide range of Weber numbers. Another comparison is conducted for the droplet maximum spreading diameter. In this case, the maximum spreading factor of the droplet is defined as $\beta_{max} = D_{max}/D_0$, where $D_{\max}$ is the droplet maximum spreading diameter. The simulation results are compared with experiments (Biance *et al.* [51], represented by solid square symbols, and Riboux *et al.* [54], by solid circle symbols) as well as the power law fitting equation (solid line) $\beta_{max} = \alpha We^{0.25}$, where the pre-factor $\alpha = 0.85$ is achieved by the experimental fitting [51]. We also compare our results with the energy balance based theoretical equation (dashed line in the figure) for $\beta_{\max}$, where [55]:

$$(\beta_{max}^2 - 1)^{0.5}\left(\frac{\sqrt{We}}{Oh}\right)^{-0.2} = \frac{\sqrt{We}}{\sqrt{We} + 7.6}. \tag{17.}$$

As presented in Figure 5(c), our simulation results are in line with the power-law fitting and theoretical equations, for a wide range of Weber numbers. It can be found that $\beta_{\max}$ in our simulations is somewhat lower than the experimental results at larger Weber numbers. This is because, in our simulations, a fixed viscosity is used and the viscous effects are overestimated for high Weber number cases, which results in a lower $\beta_{\max}$.

3. Results and discussion

3.1 Simulation setup

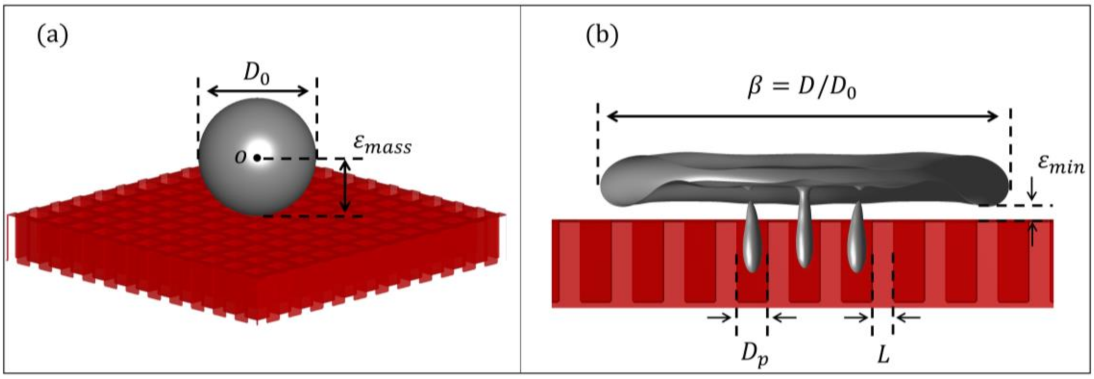

Figure 6. Illustrations of the simulation configuration (a) 3D main view of droplet initial state. (b) half cutaway view during the droplet evolution.

Having validated our multiphase thermal LB model within the ULBM framework against experimental and theoretical results, we then simulate a droplet with $D_0 = 1.7$ mm impacting on an overheated plate with square pores, with a corresponding Bond number $Bo = 0.12$. The simulation configuration is shown in Figure 6(a). In the following, the simulation domain is set as a $700 \times 700 \times 720$ box. The other setups (e.g., initial droplet radius, thermal properties of the fluid and boundary conditions) kept exactly the same as the validation cases in Sec. 2.3.

The detailed structure of the plate with square pores is shown in Figure 6(b). The depth of the pores (H_p) is kept as 40 in lattice unit (0.8 mm), and the diameter of the equal size pores is D_p, the intervals between the pores are L. In the following simulations, Jacob number is kept higher than 0.5 to ensure the plate temperature is over the Leidenforst point. It also needs to be mentioned that the minimum thickness of the vapour layer between the liquid and solid plate (the minimum distance of the liquid above the plate to the plate's upper surface, ε_{min} in the figure) is recorded. The droplet spreading factor during the evolution is defined as $\beta = D/D_0$.

3.2 The influence of Weber number

Firstly, we aim to investigate the influence of the impact Weber number at various plate temperatures and configurations. In this section, D_p and L are fixed as 11 lattices (220 μm) and 4 lattices (80 μm), respectively. Two different plate temperatures are considered: one with Jacob number Ja = 0.52 for $T_h \approx$ 400 °C and the other with Jacob number Ja = 0.7 for $T_h \approx$ 500 °C. The other simulation setups kept the same as in Sec. 2.3. We change the impact Weber numbers from 4.6 to 87.4 by changing the droplet initial velocities. Evolutions of the droplet shape are shown in Figure 7. For ease of comparison and observation, the droplet is shown as a half cutaway view, and a main view snapshot of the droplet is shown in the last frame.

Figure 7(a) demonstrates the evolution of Leidenfrost droplet impact on a flat plate. It is noticed that an air pocket is formed during the droplet spreading ($t/\tau = 0.35$), which has also been observed in previous simulations and experiments [56,57]. The trapped air in the pocket is caused by the droplet evaporation during the spreading, and the pocket-like geometry of the vapour is attributed to the effect of buoyancy force [29]. The pocket neck breaks ($t/\tau = 0.35$, marked by black dash circles) owing to the different flow scales within the droplet and the trapped air in air pocket [56]. This consequently levitates the droplet from the plate and exhausts the entrapped air. Nevertheless, the levitated droplet re-contacts the plate during the recoiling period and then completely bounces off from the plate when $t/\tau = 0.87$. Figure 7(b) shows the droplet impact on an overheated porous plate at the same Weber number and Jacob number. As shown in the figure, the droplet demonstrates similar morphologies during its evolution. However, it can be observed that a part of the droplet penetrates into the pores ($t/\tau = 0.04$) and then evaporates ($t/\tau = 0.2$). The generated vapor layer ($t/\tau = 0.36$) is thicker and the droplet rebounds faster ($t/\tau = 0.78$) in this case than the case with a flat plate.

The droplet demonstrates different morphologies when impacting the overheated porous plate at a larger Weber number. As shown in Figure 7(c), owing to a higher Weber number, more liquid penetrates into the pores at the beginning of impingement ($t/\tau = 0.042$) and evaporates. Remarkably, the droplet directly rebounds from the plate before its recoiling ($t/\tau = 0.2$) in a pancake shape. Additionally, a similar pancake-like bouncing phenomenon has also been observed in the previous experiments for droplet impact on high-temperature nanotube surfaces [21,23], heated surfaces under the depressurized environment [58], superheated micropillars surfaces [59,60] as well as superheated micropores surfaces [20]. Besides, this pancake bouncing phenomenon can also be observed when a droplet impacts a higher temperature porous plate, as shown in Figure 7(d).

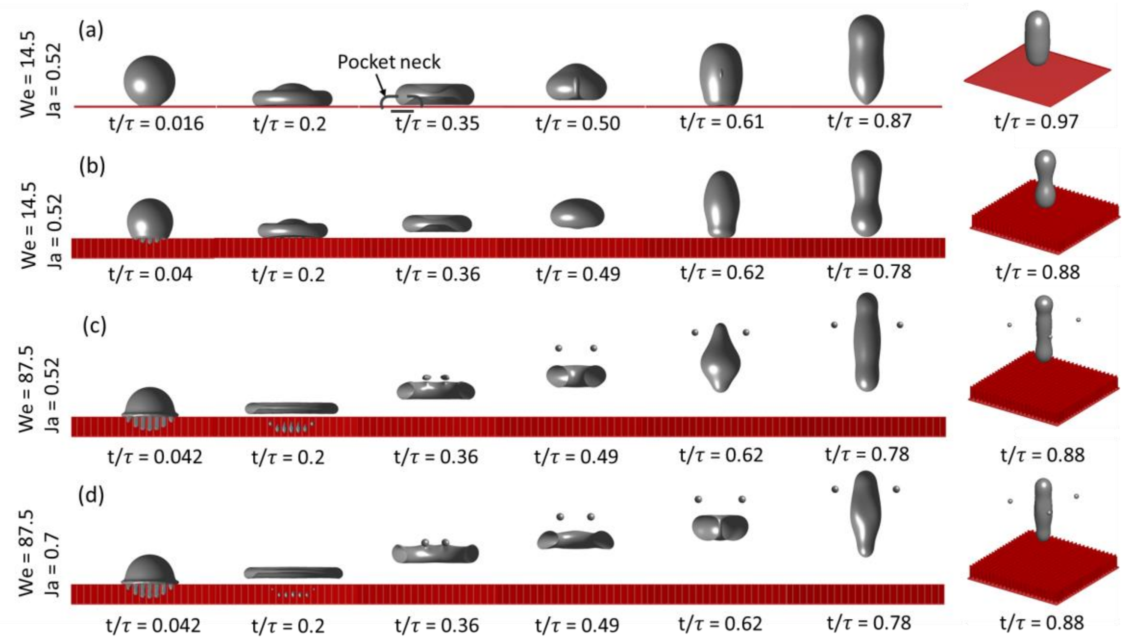
(a)
We = 14.5
Ja = 0.52
Pocket neck
t/τ = 0.016
t/τ = 0.2
t/τ = 0.35
t/τ = 0.50
t/τ = 0.61
t/τ = 0.87
t/τ = 0.97
(b)
We = 14.5
Ja = 0.52
t/τ = 0.04
t/τ = 0.2
t/τ = 0.36
t/τ = 0.49
t/τ = 0.62
t/τ = 0.78
t/τ = 0.88
(c)
We = 87.5
Ja = 0.52
t/τ = 0.042
t/τ = 0.2
t/τ = 0.36
t/τ = 0.49
t/τ = 0.62
t/τ = 0.78
t/τ = 0.88
(d)
We = 87.5
Ja = 0.7
t/τ = 0.042
t/τ = 0.2
t/τ = 0.36
t/τ = 0.49
t/τ = 0.62
t/τ = 0.78
t/τ = 0.88

Figure 7. Snapshots for a droplet impact on a heated plate with various *We* and *Ja*. (a) is for a droplet impacting a flat plate and (b)-(d) are for a droplet impacting a porous plate.

Then we give a detailed analysis of the mechanism of this unique bouncing phenomenon. The transient evolutions of droplet profiles (black lines), velocity vectors (white vectors, with a fixed scale to the velocity magnitude) and temperature distributions during the spreading stage are shown in Figure 8. Comparing cases with the same plate temperature but different Weber numbers (Figure 8(a) and Figure 8(b)), we find that more liquid penetrates into the heated pores during the droplet spreading stage for the larger Weber number case ($t/\tau = 0.08$ in Figure 8(b)). With the continuous evaporation of the penetrated liquid in pores, entrapped air is formed between the droplet bottom part and the heated plate. Thus, the larger the amount of evaporated liquid, the more entrapped air will be generated. In other words, the entrapped air generated by the evaporated liquid will provide a larger pressure force (comparing Figure 9(b) & (c) with Figure 9(a)). Because most of the impacting kinetic energy of the droplet has been transformed into surface energy during the spreading stage. Therefore, when the pressure force is larger than the gravity and vertical dynamic force, the droplet bounces from the plate (t/τ = 0.214 in Figure 8(b)). The same dynamics can also be found in the case with a higher Jacob number (plate temperature). As shown in Figure 8(c), similarly, we can observe the penetration and evaporation of the liquid inside the pores. In the case with a higher plate temperature, the liquid evaporation is faster. Thus, we can find the liquid disk rebounds with a higher velocity (seeing the velocity vectors in Figure 8(c) when t/τ = 0.214).

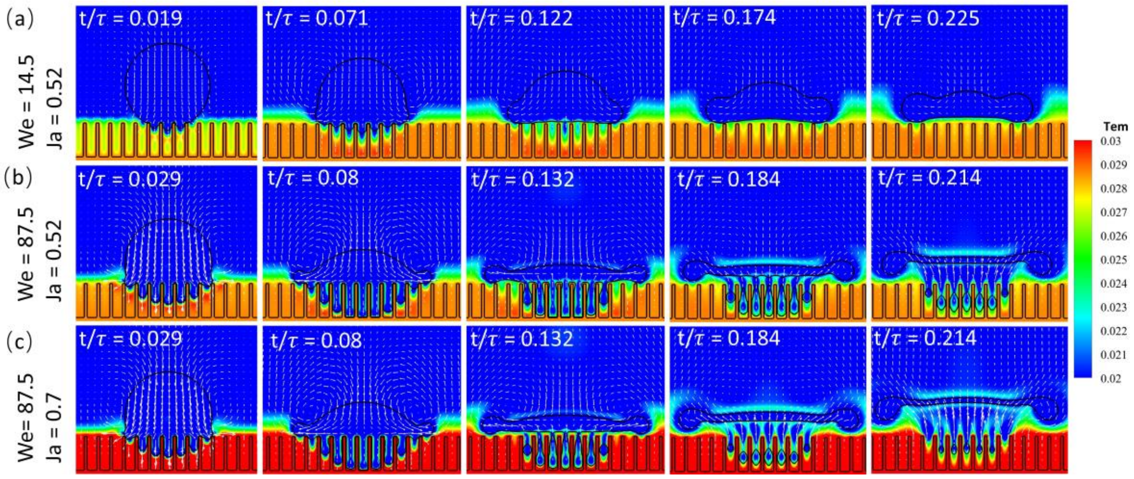

Figure 8. Illustrations of temperature distributions, velocity vectors and morphology evolutions of the droplet at the early stage of impacting a heated porous plate. (a)~(c) stands for various *We* and *Ja* cases.

Notably, satellite droplets can be observed during the droplet bounce in Figure 7 (c) and (d). The generation of the satellite droplets is owing to the breakup of thin liquid lamella during droplet spreading. A 3D main view for the selected cases is shown in Figure 10 to demonstrate the evolution of the liquid lamella. Comparing cases with a flat plate and a porous plate for the same Weber number (Figure 10 (a) and (c)), liquid flows into pore spaces, making holes in the lamella after impingement on the porous plate. Then, with the spreading of the liquid lamella, the liquid bridges between the holes break up from edges (seeing $t/\tau = 0.36$ in Figure 10 (c)), and the fragmented liquid bridges retract and form satellite droplets (seeing $t/\tau = 0.4$ in Figure 10 (c)). However, comparing cases with a porous plate but different impact Weber numbers (Figure 10 (b) and (c)), the liquid lamella remains intact for the lower Weber number case, which is due to the fewer penetrated liquid and the thicker spreading lamella.

The evolution of ε_{min}/D_0 for selected cases is recorded and plotted in Figure 11(a). As indicated in the figure, for all cases, a peak value of ε_{min} can be found before droplet recoiling. This phenomenon has also been recorded in recent simulation studies for droplet impact on an overheated flat plate [9,35,61]. The peak value of ε_{min} corresponds to the instant when the droplet kinetic energy is minimized and therefore the trapped air is exhausted. Then the droplet re-contacts the plate during the recoiling with some small oscillations. Finally, the droplet bounces from the plate. The period from the droplet's first touch on the plate to its bounce off the plate is defined as the contact time (t_c). As shown in Figure 11 (a), the peak value of ε_{min} increases slightly with the Weber number for droplet impact on a flat surface (FS). Nevertheless, ε_{min} increases significantly with the Weber number for droplet impact on a porous surface (PS). This implies the additional lift force provided by the entrapped air is similar in cases for droplet impact on a flat surface. On the contrary, the additional lift force increases significantly with the Weber number in cases of droplet impact on a porous surface. This is attributed to the evaporated liquid inside the pores. Consistent with the qualitative results, it can be found that the droplet directly bounces off from the plate during the spreading stage for the larger Weber number cases in the porous plate.

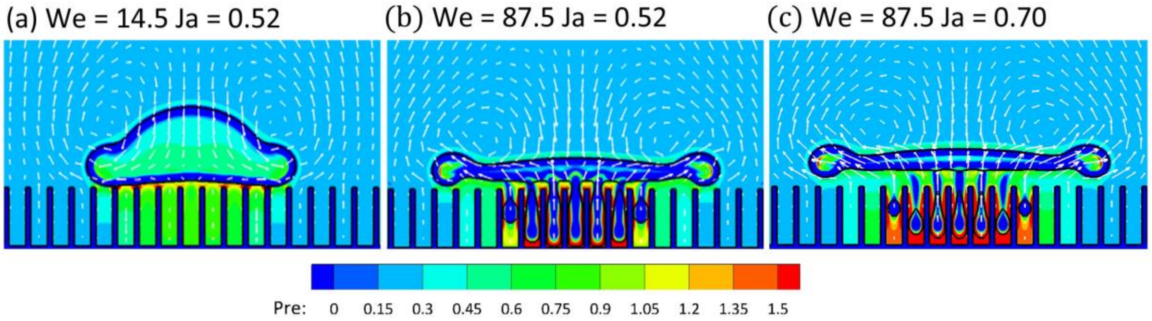

Figure 9. Illustrations of pressure distributions, velocity vectors and morphologies of a Leidenfrost droplet impacting heated porous plate at t/τ = 0.13. (a)~(c) stand for various *We* and *Ja* cases. The pressure in the figure is normalized by P_c.

We also record the evolution of ε_{mass} and plot the evolution of ε_{mass}/D_0 in Figure 11(b), whose value can be used to quantify the speed of droplet retraction and bouncing. As shown in the figure, after the droplet touches the plate, ε_{mass} decreases from the centre of the sphere ($\varepsilon_{mass}/D_0 = 0.5$) to a minimum value. Besides, it can be found that the decay rate and the minimum value of ε_{mass} are almost the same in cases with the same Weber number, regardless of different Jacob numbers and plate geometries (FS or PS). The same tendency of ε_{mass} for the same Weber number cases during the decay stage can be explained by the spreading and collapse of the droplet disk governed by the inertial effect [62]. Thus, the penetrated liquid inside the pores has little influence on the droplet spreading dynamics (comparing Figure 7 (a) and (b), at $t/\tau < 0.36$). However, the rebound velocities are different for different cases. Under the same operating conditions, it is found that the droplet rebound velocity increases with the Weber number, and the rebound velocity is always higher in the cases of droplet impact on a porous plate. This result can further reveal the fact that the pressure force generated by the evaporated liquid inside the pores contributes to the droplet bounce. As shown in the figure, we define the period between the droplet's first contact with the plate to $\varepsilon_{mass}/D_0 > 0.5$ (the initial position of ε_{mass}) as the droplet rebound time (t_r).

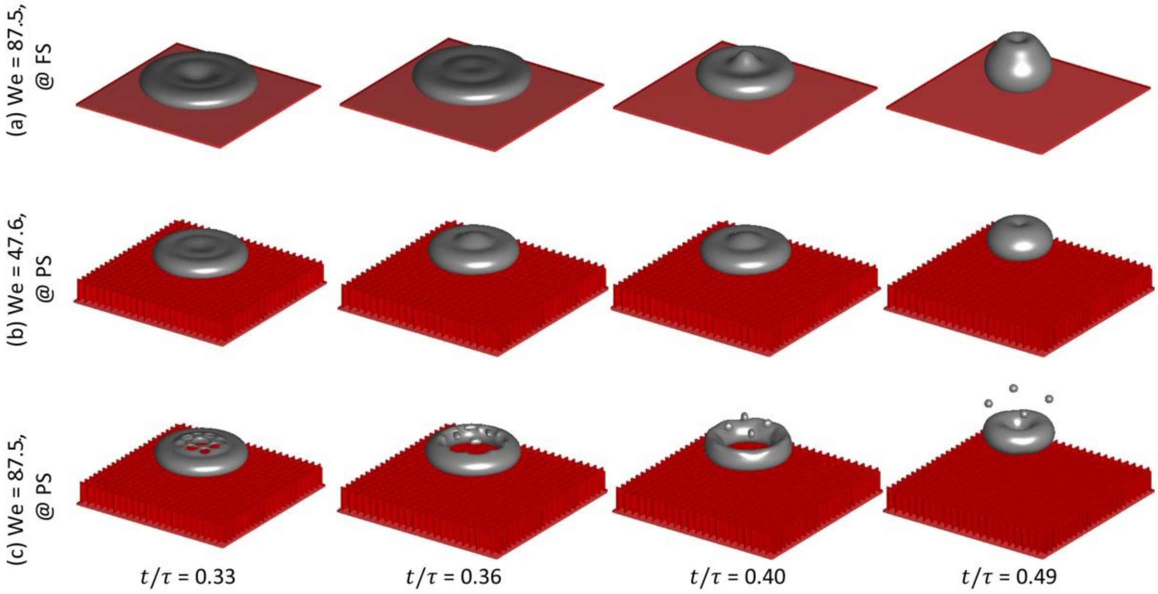

Figure 10. Illustrations of the liquid lamella evolution at *Ja* = 0.52. (a) Droplet impacts a flat plate, at *We* =87.5. (2) Droplet impacts a porous plate, at *We* =47.6. (c) Droplet impacts a porous plate, at *We* =87.5.

The dimensionless droplet contact time (t_c/τ) and droplet diameters when the droplet leaves the plate ($D(\uparrow)/D_{max}$) for all cases are recorded in Figure 12(a) and Figure 12(b), respectively. Consistent with the results in Sec. 2.3, for cases of droplet impact on a heated flat plate, dimensionless droplet contact time (t_c/τ) almost remains constant for a wide range of Weber number. as shown in Figure 12(a). For droplet impact on a porous plate at the same Jacob number (hollow triangle cases in Figure 12(a)), it always presents a shorter t_c compared with droplet impact on a flat plate. Notably, a significant decrease in t_c is observed as Weber number increase, which corresponds to the pancake bouncing cases. It is also found that, with the increase of Jacob number, both t_c and the minimum Weber number for the pancake bouncing phenomenon keep decreasing. At lower Weber numbers, the lifting diameter $D(\uparrow)$ is similar for all the cases in spite of various plate geometry and plate temperature, while the pancake bouncing doubles the lifting diameter at higher Weber numbers.

It should be pointed out that the observed pancake bouncing for droplet impact on a heated porous plate has a different mechanism from the previous pancake bouncing due to the droplet impact on superhydrophobic surfaces [63–65]. For the droplet pancake bouncing on textured superhydrophobic surfaces, the lift force is provided by the capillary force. For droplet impacting a heated porous plate, as discussed above, the lift force is generated by the pressure force of the evaporated liquid (indicated in Figure 9). In addition, it is found that the penetrated liquid remains in the pores when the droplet bounces from the plate at $t/\tau = 0.2$ (seeing Figure 7 (c) and (d)), which contrasts sharply with the retracting droplet pancake bouncing when droplets impact on textured surfaces [66,67].

The evolution of normalized droplet rebound time (t_r/τ) for all cases is recorded and plotted in Figure 12(c). As shown in the figure, for all cases, t_r decreases with Weber number. This is because, for the larger Weber number case, the surface tension is smaller compared with the dynamic force, thus the droplet recoils earlier, which can be proved in Figure 11(b) (for the larger We cases, ε_{mass} reaches the minimum value earlier). Additionally, in agreement with the results in Figure 7 and Figure 12(a), impact cases on a porous plate always produce shorter t_r compared with flat plate impact cases. And t_r is further decreased for the higher Jacob number cases at the large Weber number. The results in Figure 12(c) confirm the previous analysis, where the additional lift force provided by the evaporated liquid accelerates the droplet rebound.

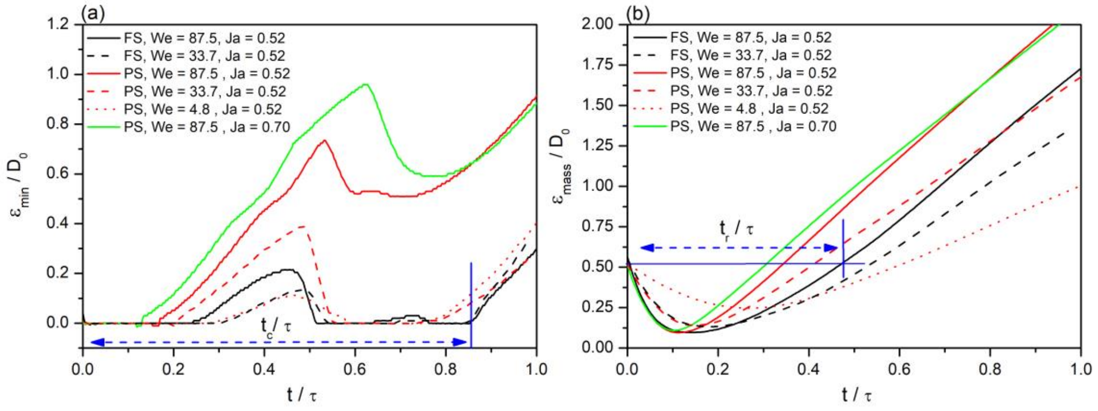

Figure 11. (a) Transient evolution of the normalized vapour layer thickness ε_{min}/D_0, different lines stand for the cases with various *We*, *Ja* and plate configurations. The period shown in the figure represents the droplet contact time (t_c). (b) Evolution of the normalized droplet gravity centre ε_{mass}/D_0 for different cases, the period shown in the figure represents the droplet rebound time (t_r).

The modified droplet maximum spreading time t_{max}/τ' (the period when the droplet reaches the maximum spreading diameter, $\tau' = (D_{max}^3\rho_l/\sigma)^{0.5}$) as a function of Weber number is plotted in Figure 13(a). It indicates that t_{max}/τ' is almost identical for different cases at the same Weber number, and t_{max}/τ' indicates a power-law decay dependency with the increase of Weber number. In the study of Lin *et al.* [68], they proposed the following equation to predict t_{max} :

$$\frac{t_{max}}{(\mathrm{D}^3_{\mathrm{max}}\rho_l/\sigma)^{0.5}} = \xi We^{-0.43}, \tag{18.}$$

where ξ is the experiment fitting constant. It should be noticed that the term $(D^3_{max}\rho_l/\sigma)^{0.5}$ on the right-hand side of Eq. (18) can be regarded as the modified inertia-capillarity time (τ') referring to a droplet of size D_{max}. The experimentally fitted universal value for ξ is 0.44 in Ref. [68] and the corresponding equation is plotted in Figure 13(a) for comparison. By fitting our simulation results in Figure 13(a), we can see, our simulation results also follow the $\sim We^{-0.43}$ power law dependency. Note that, our fitted prefactor ξ = 0.55 is slightly higher than the experimental value, which however matches the high viscosity cases in Ref. [68].

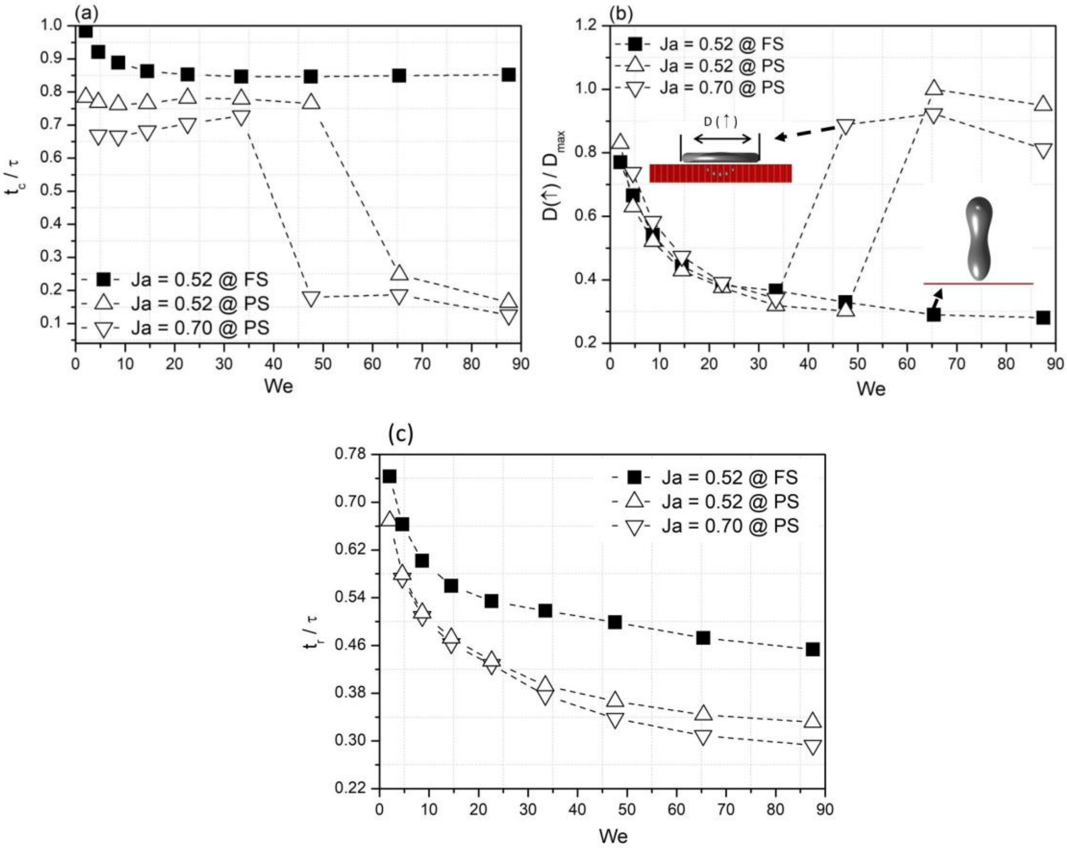

Figure 12. Normalized (a) droplet contact time t_c/τ, (b) the droplet diameters when it leaves the plate $D(\uparrow)/D_{max}$, and (c) droplet rebound time t_r/τ as a function of impacting *We* for the cases with various *Ja* and plate morphologies.

Figure 13(b) demonstrates β_{max} as a function of Weber number for all cases. Consistent with the results in Figure 13(a), it can be found that both Jacob number and plate geometries almost have no influence on β_{max}. For all cases, β_{max} increases with Weber number with a power law dependency. The best fitted equation for β_{max} in our study is:

$$\beta_{max} = 1.05\mathrm{We}^{0.17}, \tag{19.}$$

where the perfector 1.05 is in good agreement with the fitted experimental results in Ref. [51] but the index 0.17 is slightly lower than 0.25 in the experiment. We also plot the theoretical prediction Eq. (17) as the dashed line in the figure and it can be observed all simulation results are in line with the theoretical equation. Notably, for the same reason as pointed out in Sec. 2.3, the simulated β_{max} is lower than the theoretical value at the larger Weber numbers. In addition, this leads to a lower index in our best fitted exponential equation than that in Ref. [51].

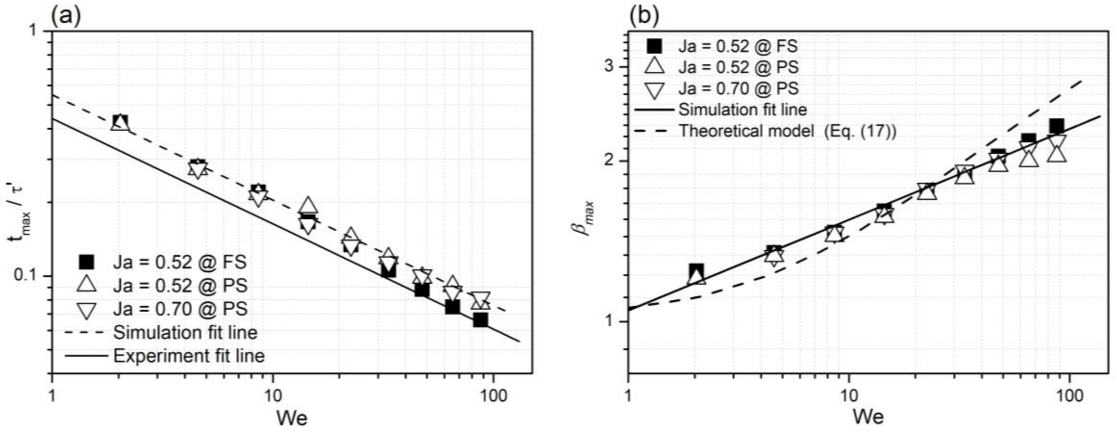

Figure 13. (a) The modified droplet maximum spreading time t_{max}/τ', where $\tau' = (D_{max}^3\rho_l/\sigma)^{0.5}$, (b) droplet maximum spreading factor β_{max} as a function of impacting We, the different symbols in the figure indicates various Ja and plate configurations. The lines in the figure stand for the theoretical prediction equations and fitted power law function.

Finally, the dimensionless droplet evaporation mass (M_e/M_0) and the averaged heat flux ($Q_{avg.}$) during the period $t = 0 \sim t_r$ are plotted in Figure 14(a) and Figure 14(b), respectively. The heat flux of each time instant is calculated as:

$$q = \frac{1}{L_xL_y}\iint \left[-\lambda\left(\frac{\partial T}{\partial z}\right)|_{(z=H_p)}\right] dxdy, \tag{20.}$$

where L_x and L_y are the length of the simulation domain in x and y directions, respectively. As shown in Figure 14(a), M_e/M_0 almost increases linearly with Weber numbers, and the evaporation mass is almost the same for two different Jacob number cases. A cylinder model is used to explain the linear relationship between M_e/M_0 and Weber number. We assume the maximum deformation of the droplet in the horizontal direction still follows $r_{max} \sim We^{0.25}$ dependency as reported in Refs. [51,69]. Besides, as mentioned above, the collapse of the droplet disk is governed by the inertial effect, and the dynamic force is minimized when $\mathrm{t} = t_{max}$. Thus, the maximum penetration length of the liquid slug inside the pores has the relationship of $h_{max} \sim U t_{max} \sim We^{0.445}$, where t_{max} is described as Eq. (18). Considering the penetrated liquid (M_p) can be regarded as a cylinder shape and be completely evaporated owing to the high plate temperature and small pores size ($D_p/D_0 < 0.1$), the evaporation mass can be scaled as $M_e/M_0 = M_p/M_0 \sim h_{max} r_{max}^2 \sim We^{0.945} \approx We$. For the time averaged heat flux shown in Figure 14(b), $Q_{avg.}$ generally increases with Weber number, which can be explained by the fact that a higher We leads to a higher liquid contact area (larger β_{max}) and a higher spreading velocity (shorter t_{max}). Consequently, this enhances the phase change heat transfer and convective heat transfer. Considering β_{max} and t_{max} are almost the same for various Jacob number at the same Weber number, it can be understood that the higher plate temperature cases demonstrate higher heat flux.

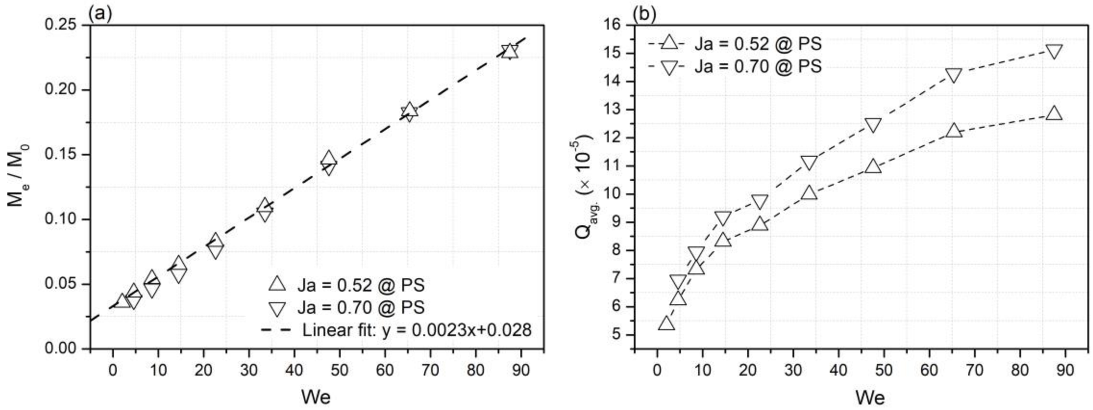

Figure 14. The relation of (a)the dimensionless droplet evaporation mass M_e/M_0 and (b) time averaged heat flux $Q_{avg.}$ with a variety of impacting We. The results are for droplet impact on a heated porous plate with different Ja, from $t = 0 \sim t_r$. The dashed line in (a) represents a linear fitting function.

3.3 The influence of pore intervals

In this section, we investigate the influence of the pore intervals. In the following simulations, D_p is fixed as 9 lattices (180 μm), and L is changed from 1 lattice (20 μm) to 97 lattices (1.9 mm), which leads to the dimensionless pore intervals $L^* = L/D_0$ varying from 0.01 to 0.99. For all the cases in this section, Weber number We = 69.2 and Jacob number Ja = 0.7, and all the other setups are the same as in Sec. 3.2.

Figure 15 shows qualitative evolutions of the droplet shape as it impacts porous plates with various $L*$. Similar to the results in Figure 7, after the droplet impacts the porous surface, a part of the droplet penetrates into the pores and evaporates. After that, the droplet levitates from the plate during the spreading and the entrapped air is exhausted. As indicated in the figure, for the smaller L^* case (Figure 15(a)), owing to the smaller solid fraction, more liquid penetrates into the pores and evaporates. As pointed out in the above analysis, the more evaporated liquid, the larger pressure force will be provided. Consequently, the droplet presents the pancake bouncing for the smaller L^* cases (similar to the phenomena in Figure 7(c) and (d)). For the larger L^* cases (Figure 15(b) and (c)), it can be observed that the droplet re-touches the plate during the recoiling stage and then bounces from the plate, which is similar to the morphologies in Figure 7(b).

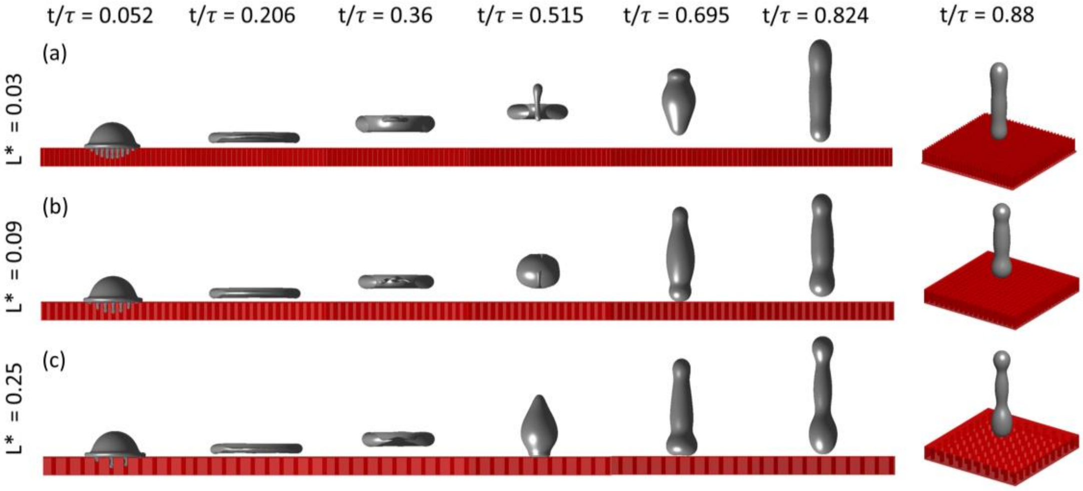

Figure 15. Qualitative evolutions of droplet impact on a porous plate with various pore intervals L^*, $We = 69.2$ and $Ja = 0.7$. (a) $L^* = 0.03$, (b) $L^* = 0.09$ and (c) $L^* = 0.25$.

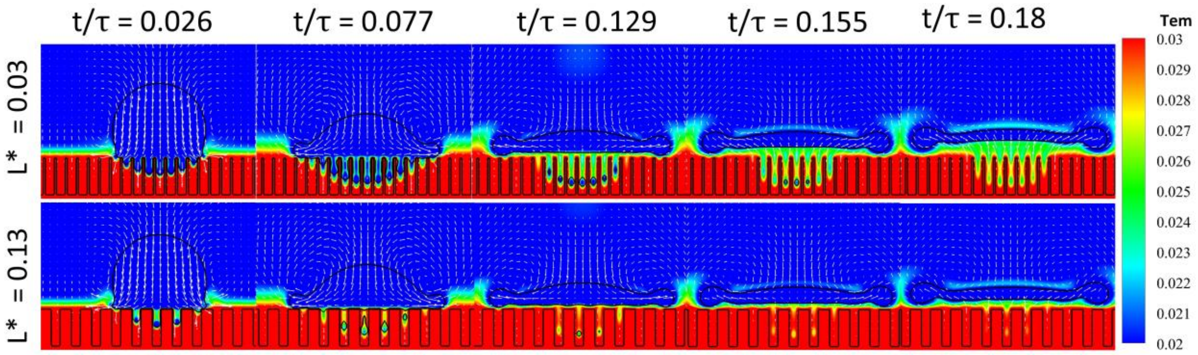

Figure 16. The temperature contours, velocity vectors and morphology evolutions of the droplet at the early stage of impact on a heated porous plate with different pore intervals.

The early stage evolutions for two different L^* cases are shown in Figure 16. Consistent with the previous findings, regarding the lower L^* case, more liquid penetrates into the pores ($t/\tau = 0.077$ in Figure 16(a)) and then evaporates ($t/\tau = 0.129$ in Figure 16(a)).

Qualitatively, it can be found that the droplet morphologies for various L^* cases are similar in the early spreading stage. Nevertheless, the larger quantity of evaporated liquid provides a larger pressure force and finally leads to the droplet bouncing from the plate ($t/\tau = 0.18$ in Figure 16(a)). It can also be confirmed by the temperature field inside the pores that for the lower L^* case, the temperature is lower due to the more significant evaporation cooling effect by its larger evaporation rate.

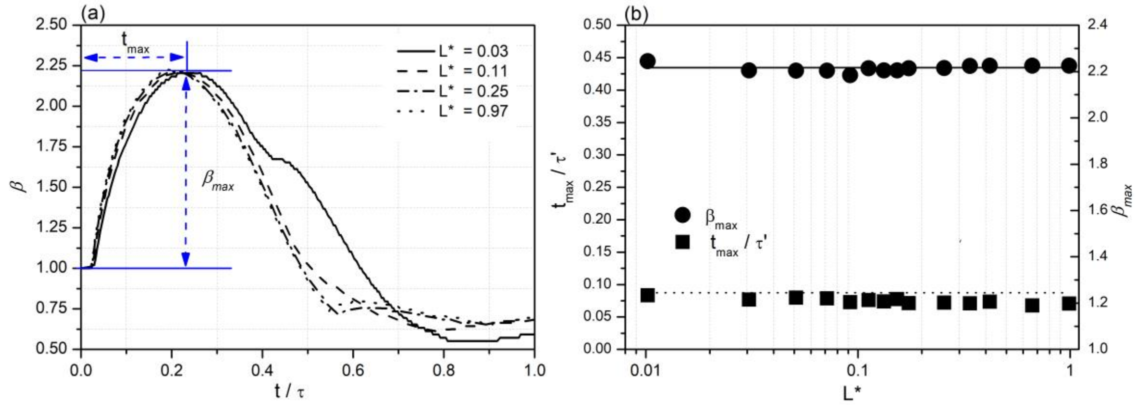

Figure 17. (a) Transient evolution of droplet spreading ratio β for various L^* cases. (b) t_{max}/τ' (right axis) and β_{max} (left axis) as a function of L^*, the dashed line and solid line stand for the predicted value calculated by Eq. (18) and Eq. (19), respectively.

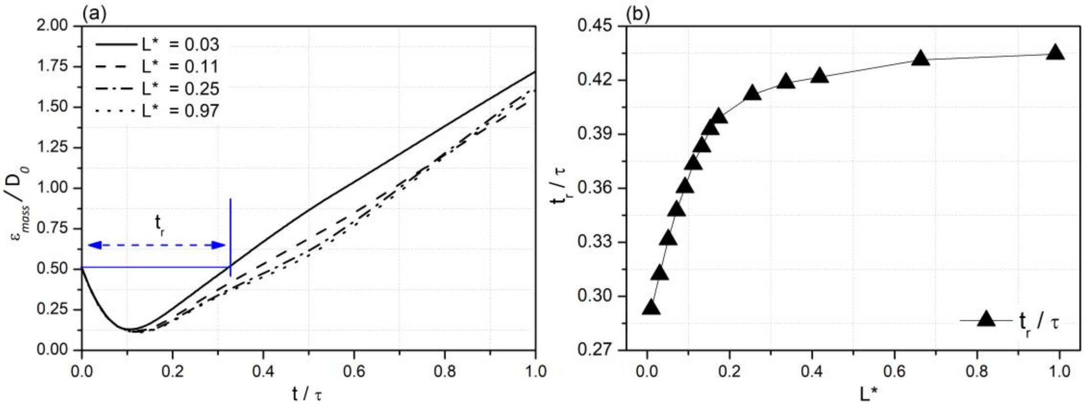

Figure 18. (a) Transient evolution of ε_{mass}/D_0 and (b) normalized t_r as a function of L^* for the droplet impact on an overheated porous plate with various L^*.

The transient evolution of droplet spreading ratio for various L^* cases are plotted in Figure 17(a). As shown in the figure, the droplet first spreads to the maximum value and then recoils. Concurring with the qualitative results in Figure 16, the spreading ratio is identical for a wide range of L^*. β_{max} (left axis, represented by solid squares) and t_{max}/τ' (right axis, represented by solid circles) in relation of L^* is plotted in Figure 17(b). As shown in the figure, consistent with the qualitative observation in Figure 15, both β_{max} and t_{max}/τ' are almost at a constant value for a wide range L^*, which can be observed in Figure 17(a). The identical β_{max} and t_{max} can be explained by the fact that the droplet spreading stage is dominated by the inertia effect. In other words, the penetrated liquid inside pores has little influence on the droplet dynamics in the horizontal direction. Consequently, β_{max} and t_{max} present similar values under the same Weber number, regardless of different values of L^*. Additionally, the predicted value of t_{max} by Eq. (18) and β_{max} by Eq. (19) are plotted in Figure 17(b) by dashed and solid lines, respectively. It can be observed that the theoretical equations can also give good predictions of β_{max} and t_{max} for a wide range of L^*.

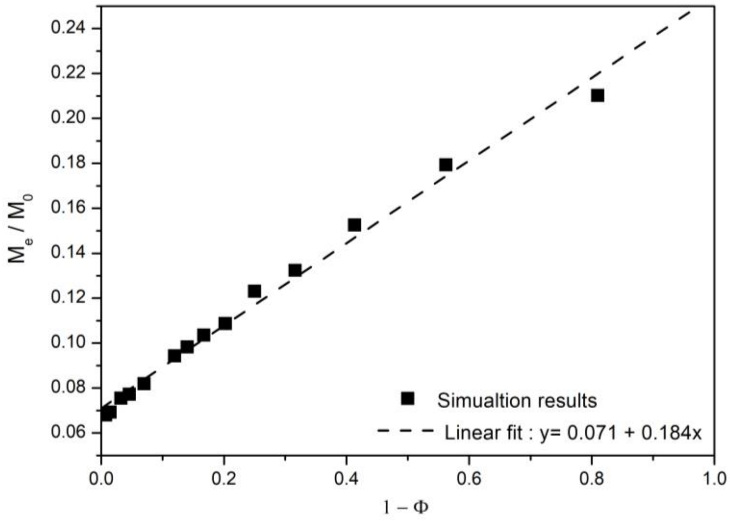

Figure 19. Normalized droplet evaporated mass as a function M_e/M_0 of surface solid fraction *1-* ϕ, the dashed line in the figure represents the linear fitting function.

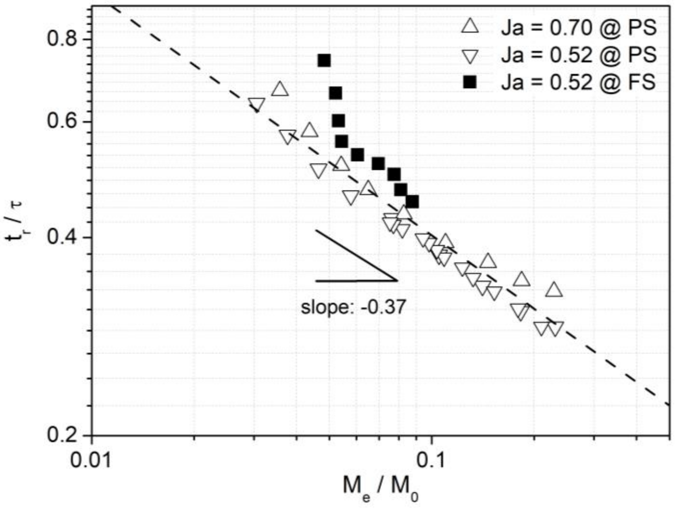

Figure 20. Dimensionless droplet rebound time t_r/τ as a function of normalized droplet evaporated mass M_e/M_0 for all cases, the dashed line in the figure represents the power law fitting function.

The evolution of ε_{mass}/D_0 is plotted in Figure 18(a), and t_r/τ as a function of L^* is shown in Figure 18(b). It can be observed that the evolution of ε_{mass} during the decay stage for all cases is almost constant. During the rebound stage, the minimum L^* presents the fastest rebound speed and shortest rebound time (t_r). For the larger L^* cases during the rebound stage, the evolutions of ε_{mass} are very similar (e.g., $L^* = 0.25$ and $L^* = 0.97$). It should be mentioned that the solid fraction of the porous plate can be calculated as $\phi = 1 - (D_p/(D_p + L))^2$, D_p is fixed as 9 lattices when changing L. As a result, the corresponding ϕ varies from 0.9 to 0.99 when L* is changed from 0.2 to 0.97, which implies that only a small amount of liquid penetrates into the pores when $L^* > 0.2$, and the amount of the evaporated liquid is very small. Consequently, the pore intervals have slight influence on droplet dynamics. For a similar reason, we can find t_r remains at a similar value when $L^* > 0.2$ (As shown in Figure 18(b)). This can also explain why β (Figure 17(a)) and ε_{mass} (Figure 18(a)) present similar evolution trends for the high L^* cases.

We record M_e/M_0 ($t = 0 \sim t_r$) as a function of the plate opening fraction $1 - \phi$ in Figure 19. As shown, M_e/M_0 is linearly increased with $1 - \phi$. Additionally, we can find M_e is significantly increased with $1 - \phi$ when $1 - \phi > 0.1$ ($L^* < 0.2$); thus, it explains why t_r is dramatically increased when $L^* < 0.2$ (as shown in Figure 18(b)). Finally, we plot the dimensionless droplet rebound time t_r/τ as a function of M_e/M_0 for all cases in Figure 20. As shown in the figure, the droplet rebound time decreases with increasing evaporation mass. In simulations of droplet impact on a porous plate, the maximum evaporation mass is higher and the minimum rebound time is smaller than the corresponding values in the flat-plate cases for the same range of Weber numbers. Remarkably, t_r/τ can be fitted by a ~ $(M_e/M_0)^{-0.37}$ for the cases of droplet impact on a porous plate. However, the cases of droplet impact on a flat plate clearly deviate from the power law dependency. The results for the cases of droplet impact on a porous plate demonstrate, the droplet penetration into the pores leads to a larger quantity of evaporation mass, which generates an additional lift force and accelerates the rebound of the droplet, leading to a short t_r. It should be pointed out that, in our simulations, the pore size D_p is relatively small ($D_p/D_0 \approx 0.1$) and thus the liquid in the pores can fast evaporate. As pointed out in the above analysis, the evaporated liquid is critical to the droplet bouncing dynamics, and the droplet could present different dynamics when the liquid in the pores evaporates to a different extent. Thus, it is necessary to extend the simulation to a wider range of surface configurations and operating parameters in future studies.

4. Conclusion

In this study, the unified lattice Boltzmann model (ULBM) is applied to numerically investigate droplet impact on a porous plate above the Leidenfrost temperature. The ULBM with the KBC collision operator is firstly validated by reproducing theoretical and experimental results of benchmark cases as well as results of Leidenfrost droplet impingement on a flat plate. Then, we simulate the Leidenfrost droplet impingement on a plate with square pores. Effects of the droplet impacting Weber number, the plate temperature (Ja) and the plate configuration (flat plate, porous plate, and different pore intervals L) on droplet dynamics are revealed. The following conclusions can be drawn:

(1) In cases with small Weber numbers, the Leidenfrost droplet impact on a porous plate shows similar bouncing morphologies as it impinges on a flat plate. On the other hand, in cases with large Weber numbers, a part of the droplet penetrates into the pores and evaporates. The vapour formed from the liquid evaporation provides additional lift force. This subsequently causes the droplet rebound in a pancake shape before its recoil, which breaks the theoretical Rayleigh's limitation and reduces the droplet contact time (t_c) significantly.

(2) Compared with the droplet impact on a flat plate, the droplet impact on a porous plate shows a faster rebound time (t_r). The increase of plate temperature and Weber number promotes the droplet rebound, and the increasing Jacob number decreases the minimum Weber number for the pancake bouncing phenomena.

(3) The modified droplet maximum spreading time (t_{max}) and maximum spreading factor ($\beta_{\max}$) are similar in cases with the same Weber number but various plate geometries and Jacob numbers. The evolution of $t_{max}/\ (D_{max}^3 \rho_l/\sigma)^{0.5}$ and $\beta_{\max}$ can be predicted by the power law functions of Weber number in Eq. (18) and Eq. (19), respectively. For the cases of droplet impact on a porous plate, the evaporated liquid mass linearly increases with Weber number.

(4) When changing the pore intervals, values of t_{max} and $\beta_{\max}$ keep almost unchanged and still follow the proposed power law functions [Eqs. (18) and (19)]. It is found that the droplet rebounds faster in cases with smaller normalized pore intervals L^*. In cases with the larger normalized pore intervals ($L^* > 0.2$), both the droplet transient evolution and the rebound time (t_r) are similar.

(5) Owing to the small pore size ($D_p/\ D_0 \sim 0.1$), the part of the droplet that is inside the pores evaporates rapidly. Therefore, the normalized droplet evaporation mass (M_e/M_0) is proportional to the plate opening fractions (1- ϕ). The results indicate that, for droplet impact on a porous plate, the droplet rebound time can be fitted as a power law decay function of the normalized droplet evaporation mass.

Acknowledgements

This work was supported by the UK Engineering and Physical Sciences Research Council (EPSRC) under the project “UK Consortium on Mesoscale Engineering Sciences (UKCOMES)” (Grant No. EP/R029598/1) and the project “Exascale Computing for System-Level Engineering: Design, Optimisation and Resilience” (Grant No. EP/V001531/1).

Bibliography

[1] G. Liang and I. Mudawar, *Review of Spray Cooling – Part 1: Single-Phase and Nucleate Boiling Regimes, and Critical Heat Flux*, Int. J. Heat Mass Transf. **115**, 1174 (2017).

[2] G. Liang and I. Mudawar, *Review of Spray Cooling – Part 2: High Temperature Boiling Regimes and Quenching Applications*, Int. J. Heat Mass Transf. **115**, 1206 (2017).

[3] T. M. Anderson and I. Mudawar, *Microelectronic Cooling by Enhanced Pool Boiling of a Dielectric Fluorocarbon Liquid*, J. Heat Transfer **111**, 752 (1989).

[4] D. Quéré, *Leidenfrost Dynamics*, Annu. Rev. Fluid Mech. **45**, 197 (2013).

[5] V. S. Ajaev and O. A. Kabov, *Levitation and Self-Organization of Droplets*, Annu. Rev. Fluid Mech. **53**, 203 (2021).

[6] G. Liang and I. Mudawar, *Review of Drop Impact on Heated Walls*, Int. J. Heat Mass Transf. **106**, 103 (2017).

[7] V. K. Dhir, *BOILING HEAT TRANSFER*, Annu. Rev. Fluid Mech. **30**, 365 (1998).

[8] S. Ernest and P. R. S. R. August, *VI. On the Capillary Phenomena of Jets*, Proc. R. Soc. London **29**, 71 (1879).

[9] D. Chatzikyriakou, S. P. Walker, G. F. Hewitt, C. Narayanan, and D. Lakehal, *Comparison of Measured and Modelled Droplet-Hot Wall Interactions*, Appl. Therm. Eng. **29**, 1398 (2009).

[10] D. Richard, C. Clanet, and D. Quéré, *Contact Time of a Bouncing Drop*, Nature **417**, 811 (2002).

[11] Z. Hu, F. Chu, Y. Lin, and X. Wu, *Contact Time of Droplet Impact on Inclined Ridged Superhydrophobic Surfaces*, Langmuir **38**, 1540 (2022).

[12] Z. Hu, F. Chu, and X. Wu, *Double-Peak Characteristic of Droplet Impact Force on Superhydrophobic Surfaces*, Extrem. Mech. Lett. **52**, 101665 (2022).

[13] G. Lagubeau, M. Le Merrer, C. Clanet, and D. Quéré, *Leidenfrost on a Ratchet*, Nat. Phys. **7**, 395 (2011).

[14] A. Bouillant, T. Mouterde, P. Bourrianne, A. Lagarde, C. Clanet, and D. Quéré,

Leidenfrost Wheels, Nat. Phys. **14**, 1188 (2018).

[15] G. Graeber, K. Regulagadda, P. Hodel, C. Küttel, D. Landolf, T. M. Schutzius, and D. Poulikakos, *Leidenfrost Droplet Trampolining*, Nat. Commun. **12**, 1 (2021).

[16] F. Celestini, T. Frisch, and Y. Pomeau, *Room Temperature Water Leidenfrost Droplets*, Soft Matter **9**, 9535 (2013).

[17] H. M. Kwon, J. C. Bird, and K. K. Varanasi, *Increasing Leidenfrost Point Using Micro-Nano Hierarchical Surface Structures*, Appl. Phys. Lett. **103**, (2013).

[18] C. Kruse, T. Anderson, C. Wilson, C. Zuhlke, D. Alexander, G. Gogos, and S. Ndao, *Extraordinary Shifts of the Leidenfrost Temperature from Multiscale Micro/Nanostructured Surfaces*, Langmuir **29**, 9798 (2013).

[19] D. Arnaldo Del Cerro, Á. G. Marín, G. R. B. E. Römer, B. Pathiraj, D. Lohse, and A. J. Huis In 'T Veld, *Leidenfrost Point Reduction on Micropatterned Metallic Surfaces*, Langmuir **28**, 15106 (2012).

[20] M. Jiang, Y. Wang, F. Liu, H. Du, Y. Li, H. Zhang, S. To, S. Wang, C. Pan, J. Yu, D. Quéré, and Z. Wang, *Inhibiting the Leidenfrost Effect above 1,000 °C for Sustained Thermal Cooling*, Nature **601**, 568 (2022).

[21] M. Liu, H. Du, Y. Cheng, H. Zheng, Y. Jin, S. To, S. Wang, and Z. Wang, *Explosive Pancake Bouncing on Hot Superhydrophilic Surfaces*, ACS Appl. Mater. Interfaces **13**, 24321 (2021).

[22] X. Zhong, Y. Zhang, Y. Hou, H. Feng, and L. Sun, *Unique Dynamics of Water-Ethanol Binary Droplets Impacting onto a Superheated Surface with Nanotubes*, Int. J. Heat Mass Transf. **164**, 120571 (2021).

[23] W. Tong, L. Qiu, J. Jin, L. Sun, and F. Duan, *Unique Lift-off of Droplet Impact on High Temperature Nanotube Surfaces*, Appl. Phys. Lett. **111**, 091605 (2017).

[24] S. Lyua, H. Tan, Y. Wakata, X. Yang, C. K. Law, D. Lohse, and C. Sun, *On Explosive Boiling of a Multicomponent Leidenfrost Drop*, Proc. Natl. Acad. Sci. U. S. A. **118**, 1 (2021).

[25] S. Lyu, V. Mathai, Y. Wang, B. Sobac, P. Colinet, D. Lohse, and C. Sun, *Final Fate of a Leidenfrost Droplet: Explosion or Takeoff*, Sci. Adv. **5**, 1 (2019).

[26] Y. Ge and L. S. Fan, *Three-Dimensional Simulation of Impingement of a Liquid Droplet on a Flat Surface in the Leidenfrost Regime*, Phys. Fluids **17**, 1 (2005).

[27] D. J. E. Harvie and D. F. Fletcher, *A Hydrodynamic and Thermodynamic Simulation of Droplet Impacts on Hot Surfaces, Part I: Theoretical Model*, Int. J. Heat Mass Transf. **44**, 2633 (2001).

[28] D. J. E. Harvie and D. F. Fletcher, *A Hydrodyamic and Thermodynamic Simulation of Droplet Impacts on Hot Surfaces, Part II: Validation and Applications*, Int. J. Heat Mass Transf. **44**, 2643 (2001).

[29] I. Chakraborty, M. V. Chubynsky, and J. E. Sprittles, *Computational Modelling of Leidenfrost Drops*, J. Fluid Mech. **936**, 1 (2022).

[30] Q. Li, K. H. Luo, Q. J. Kang, Y. L. He, Q. Chen, and Q. Liu, *Lattice Boltzmann Methods for Multiphase Flow and Phase-Change Heat Transfer*, Prog. Energy Combust. Sci. **52**, 62 (2016).

[31] C. K. Aidun and J. R. Clausen, *Lattice-Boltzmann Method for Complex Flows*, Annu. Rev. Fluid Mech. **42**, 439 (2010).

[32] L. Chen, Q. Kang, Y. Mu, Y. L. He, and W. Q. Tao, *A Critical Review of the Pseudopotential Multiphase Lattice Boltzmann Model: Methods and Applications*, Int. J. Heat Mass Transf. **76**, 210 (2014).

[33] H. Huang, M. C. Sukop, and X.-Y. Lu, *Multiphase Lattice Boltzmann Methods: Theory and Application* (John Wiley & Sons, Ltd, Chichester, UK, 2015).

[34] Q. Li, Q. J. Kang, M. M. Francois, and A. J. Hu, *Lattice Boltzmann Modeling of Self-Propelled Leidenfrost Droplets on Ratchet Surfaces*, Soft Matter **12**, 302 (2016).

[35] Z. Xu, J. Li, Z. Yao, and J. Li, *Effects of Superheat Degree and Wettability on Droplet Evaporation Time near Leidenfrost Point through Lattice Boltzmann Simulation*, Int. J. Therm. Sci. **167**, 107017 (2021).

[36] N. Karami, M. H. Rahimian, and M. Farhadzadeh, *Numerical Simulation of Droplet Evaporation on a Hot Surface near Leidenfrost Regime Using Multiphase Lattice Boltzmann Method*, Appl. Math. Comput. **312**, 91 (2017).

[37] Y. Xu, L. Tian, C. Zhu, and N. Zhao, *Numerical Investigation of Droplet Impact on Heated Surfaces with Pillars*, Phys. Fluids **34**, 023305 (2022).

[38] L. Fei, J. Yang, Y. Chen, H. Mo, and K. H. Luo, *Mesoscopic Simulation of Three-Dimensional Pool Boiling Based on a Phase-Change Cascaded Lattice Boltzmann Method*, Phys. Fluids **32**, 103312 (2020).

[39] G. Wang, L. Fei, and K. H. Luo, *Unified Lattice Boltzmann Method with Improved Schemes for Multiphase Flow Simulation: Application to Droplet Dynamics under Realistic Conditions*, Phys. Rev. E **105**, 045314 (2022).

[40] L. Fei, K. H. Luo, and Q. Li, *Three-Dimensional Cascaded Lattice Boltzmann Method: Improved Implementation and Consistent Forcing Scheme*, Phys. Rev. E **97**, 053309 (2018).

[41] K. H. Luo, L. Fei, and G. Wang, *A Unified Lattice Boltzmann Model and Application to Multiphase Flows*, Philos. Trans. R. Soc. A Math. Phys. Eng. Sci. **379**, 20200397 (2021).

[42] L. Fei, J. Du, K. H. Luo, S. Succi, M. Lauricella, A. Montessori, and Q. Wang, *Modeling Realistic Multiphase Flows Using a Non-Orthogonal Multiple-Relaxation-Time Lattice Boltzmann Method*, Phys. Fluids **31**, (2019).

[43] I. V. Karlin, F. Bösch, and S. S. Chikatamarla, *Gibbs' Principle for the Lattice-Kinetic Theory of Fluid Dynamics*, Phys. Rev. E - Stat. Nonlinear, Soft Matter Phys. **90**, 1 (2014).

[44] A. L. Kupershtokh, D. A. Medvedev, and D. I. Karpov, *On Equations of State in a Lattice Boltzmann Method*, Comput. Math. with Appl. **58**, 965 (2009).

[45] P. Yuan and L. Schaefer, *Equations of State in a Lattice Boltzmann Model*, Phys. Fluids **18**, (2006).

[46] Q. Li, Y. Yu, and K. H. Luo, *Implementation of Contact Angles in Pseudopotential Lattice Boltzmann Simulations with Curved Boundaries*, Phys. Rev. E **100**, 1 (2019).

[47] Q. Li, J. Y. Huang, and Q. J. Kang, *On the Temperature Equation in a Phase Change Pseudopotential Lattice Boltzmann Model*, Int. J. Heat Mass Transf. **127**, 1112 (2018).

[48] D. Soto, H. L. Girard, A. Le Helloco, T. Binder, D. Quéré, and K. K. Varanasi, *Droplet Fragmentation Using a Mesh*, Phys. Rev. Fluids **3**, 1 (2018).

[49] G. Liang, S. Shen, Y. Guo, and J. Zhang, *Boiling from Liquid Drops Impact on a Heated Wall*, Int. J. Heat Mass Transf. **100**, 48 (2016).

[50] L. H. J. Wachters, L. Smulders, J. R. Vermeulen, and H. C. Kleiweg, *The Heat Transfer from a Hot Wall to Impinging Mist Droplets in the Spheroidal State*, Chem. Eng. Sci. **21**, 1231 (1966).

[51] A. L. Biance, F. Chevy, C. Clanet, G. Lagubeau, and D. Quéré, *On the Elasticity of an Inertial Liquid Shock*, J. Fluid Mech. **554**, 47 (2006).

[52] T. Tran, H. J. J. Staat, A. Susarrey-Arce, T. C. Foertsch, A. Van Houselt, H. J. G. E. Gardeniers, A. Prosperetti, D. Lohse, and C. Sun, *Droplet Impact on Superheated Micro-Structured Surfaces*, Soft Matter **9**, 3272 (2013).

[53] M. Kunihide and M. Itaru, *The Behavior of a Water Droplet on Heated Surfaces*, Int. J. Heat Mass Transf. **27**, 781 (1984).

[54] G. Riboux and J. M. Gordillo, *Maximum Drop Radius and Critical Weber Number for Splashing in the Dynamical Leidenfrost Regime*, J. Fluid Mech. **803**, 516 (2016).

[55] J. B. Lee, N. Laan, K. G. De Bruin, G. Skantzaris, N. Shahidzadeh, D. Derome, J. Carmeliet, and D. Bonn, *Universal Rescaling of Drop Impact on Smooth and Rough

Surfaces, J. Fluid Mech. **786**, R41 (2015).

[56] W. Yuan, T. Wei, and M. Zhang, *Dynamical Vapour Pocket of an Impacting Leidenfrost Droplet: Evaporation and Scaling Relations*, Int. J. Heat Fluid Flow **95**, 108965 (2022).

[57] T. Tran, H. J. J. Staat, A. Prosperetti, C. Sun, and D. Lohse, *Drop Impact on Superheated Surfaces*, Phys. Rev. Lett. **108**, 1 (2012).

[58] R. Hatakenaka, J. Breitenbach, I. V. Roisman, C. Tropea, and Y. Tagawa, *Magic Carpet Breakup of a Drop Impacting onto a Heated Surface in a Depressurized Environment*, Int. J. Heat Mass Transf. **145**, 118729 (2019).

[59] S. C. Park, M. H. Kim, S. Wongwises, D. I. Yu, and H. S. Ahn, *Explosive Lift-off Triggering Mechanism on a Surface with Micropillar Arrays: Liquid-Vapor Interface Behavior between Micropillars during Drop Impingement*, Appl. Therm. Eng. **201**, 117739 (2022).

[60] C. Te Huang, C. W. Lo, and M. C. Lu, *Reducing Contact Time of Droplets Impacting Superheated Hydrophobic Surfaces*, Small **2106704**, 1 (2022).

[61] L. Rueda Villegas, S. Tanguy, G. Castanet, O. Caballina, and F. Lemoine, *Direct Numerical Simulation of the Impact of a Droplet onto a Hot Surface above the Leidenfrost Temperature*, Int. J. Heat Mass Transf. **104**, 1090 (2017).

[62] G. Wang, J. Gao, and K. H. Luo, *Droplet Impacting a Superhydrophobic Mesh Array: Effect of Liquid Properties*, Phys. Rev. Fluids **5**, (2020).

[63] Y. Liu, L. Moevius, X. Xu, T. Qian, J. M. Yeomans, and Z. Wang, *Pancake Bouncing on Superhydrophobic Surfaces*, Nat. Phys. **10**, 515 (2014).

[64] Z. Hu, F. Chu, and X. Wu, *Design Principle of Ridge-Textured Superhydrophobic Surfaces for Inducing Pancake Bouncing*, Int. Commun. Heat Mass Transf. **136**, 106167 (2022).

[65] J. Song, M. Gao, C. Zhao, Y. Lu, L. Huang, X. Liu, C. J. Carmalt, X. Deng, and I. P. Parkin, *Large-Area Fabrication of Droplet Pancake Bouncing Surface and Control of Bouncing State*, ACS Nano **11**, 9259 (2017).

[66] A. Mazloomi Moqaddam, S. S. Chikatamarla, and I. V. Karlin, *Drops Bouncing off Macro-Textured Superhydrophobic Surfaces*, J. Fluid Mech. **824**, 866 (2017).

[67] Z. Hu, F. Chu, and X. Wu, *Design Principle of Ridge-Textured Superhydrophobic Surfaces for Inducing Pancake Bouncing*, Int. Commun. Heat Mass Transf. **136**, 106167 (2022).

[68] S. Lin, B. Zhao, S. Zou, J. Guo, Z. Wei, and L. Chen, *Impact of Viscous Droplets on Different Wettable Surfaces: Impact Phenomena, the Maximum Spreading Factor,*

Spreading Time and Post-Impact Oscillation, J. Colloid Interface Sci. **516**, 86 (2018).

[69] C. Clanet, C. Béguin, D. Richard, and D. Quéré, *Maximal Deformation of an Impacting Drop*, J. Fluid Mech. **517**, 199 (2004).

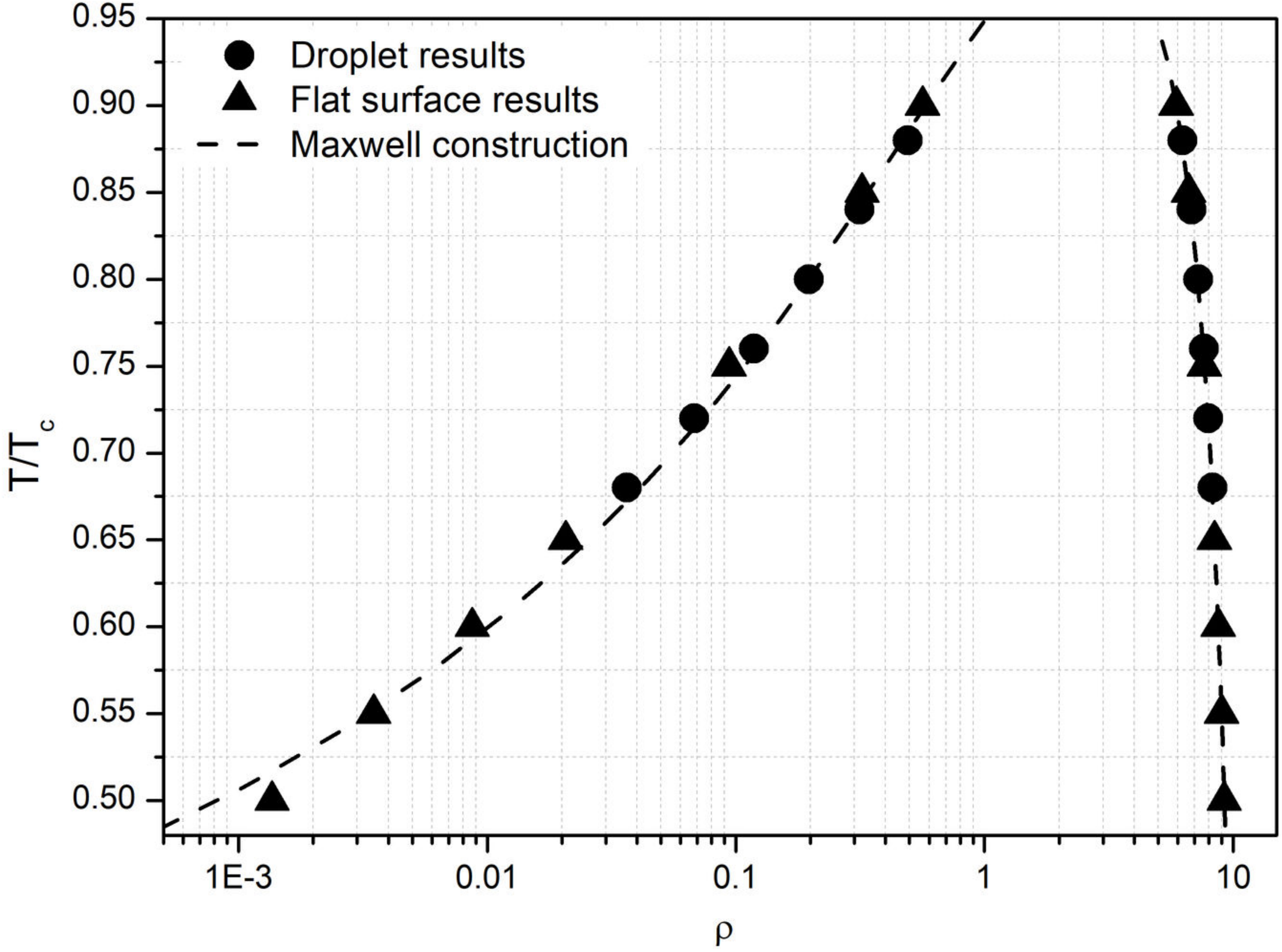

● Droplet results
▲ Flat surface results
Maxwell construction
T/T_c
0.95
0.90
0.85
0.80
0.75
0.70
0.65
0.60
0.55
0.50
1E-3
0.01
0.1
1
10
ρ

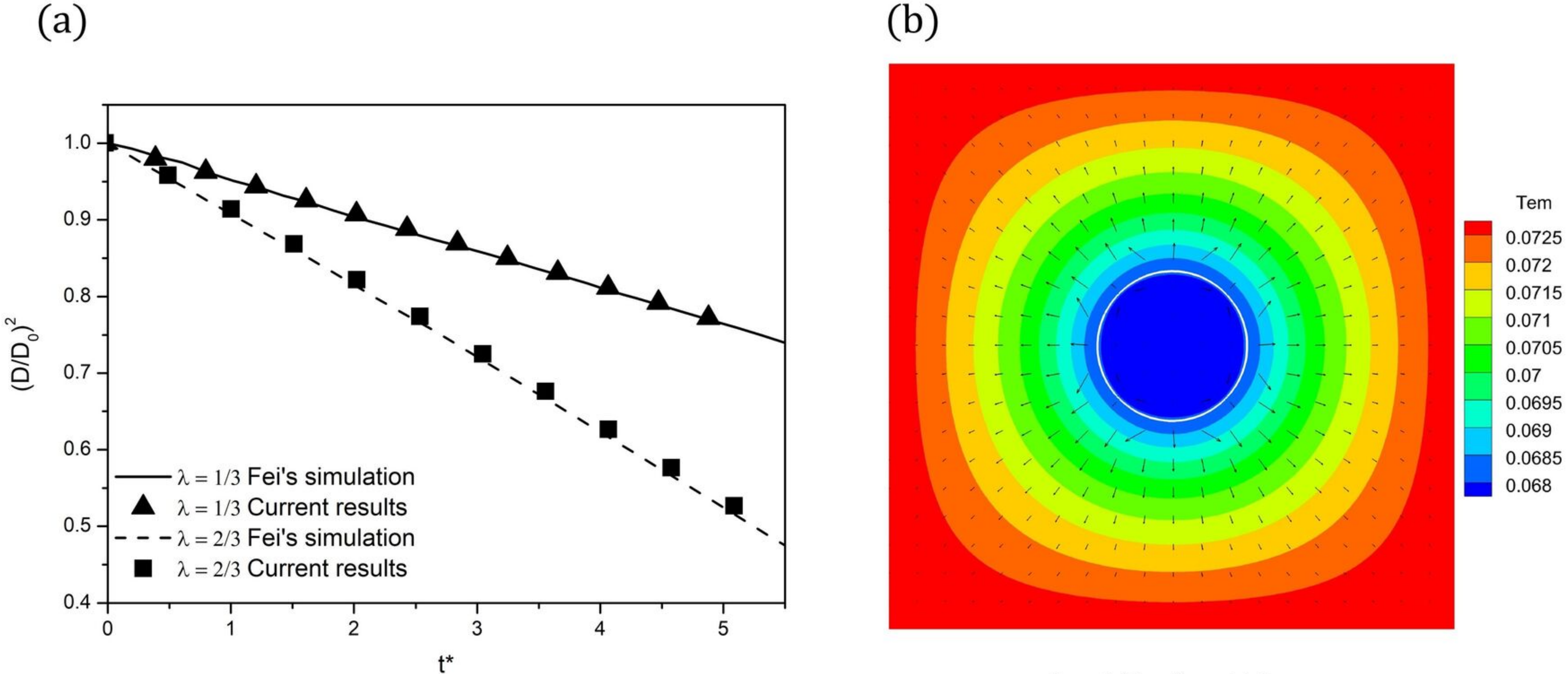
(a)
(b)
1.0
0.9
0.8
0.7
0.6
0.5
0.4
$(D/D_0)^2$
0
1
2
3
4
5
t*
$\lambda = 1/3$ Fei's simulation
$\lambda = 1/3$ Current results
$\lambda = 2/3$ Fei's simulation
$\lambda = 2/3$ Current results
Tem
0.0725
0.072
0.0715
0.071
0.0705
0.07
0.0695
0.069
0.0685
0.068

λ = 2/3, t* = 5.1

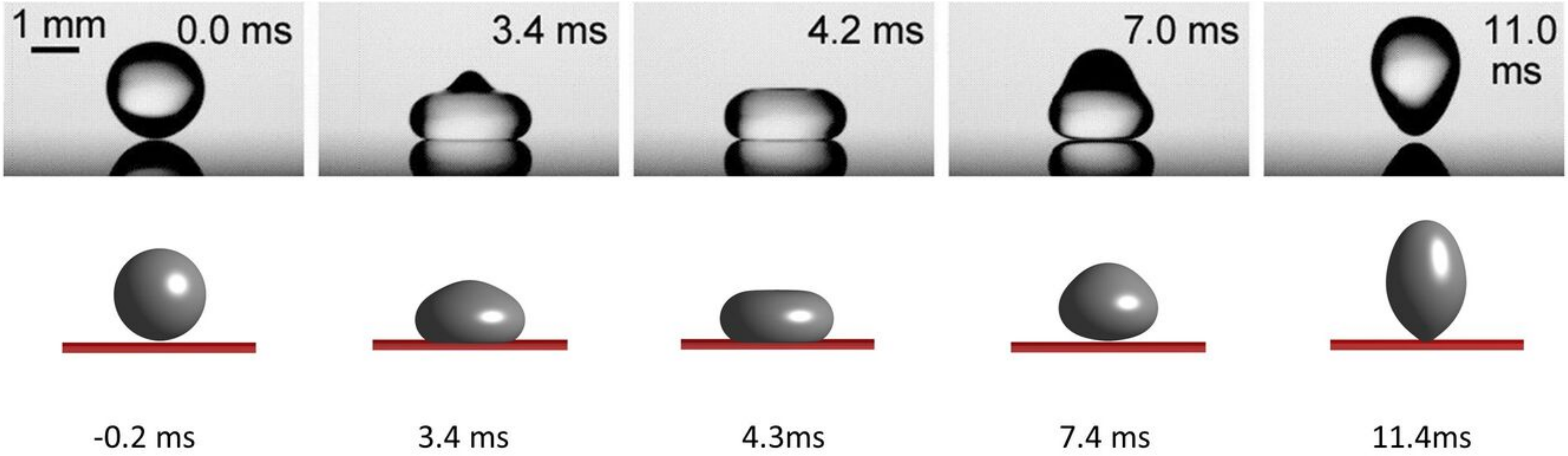
1 mm
0.0 ms
3.4 ms
4.2 ms
7.0 ms
11.0 ms
-0.2 ms
3.4 ms
4.3ms
7.4 ms
11.4ms

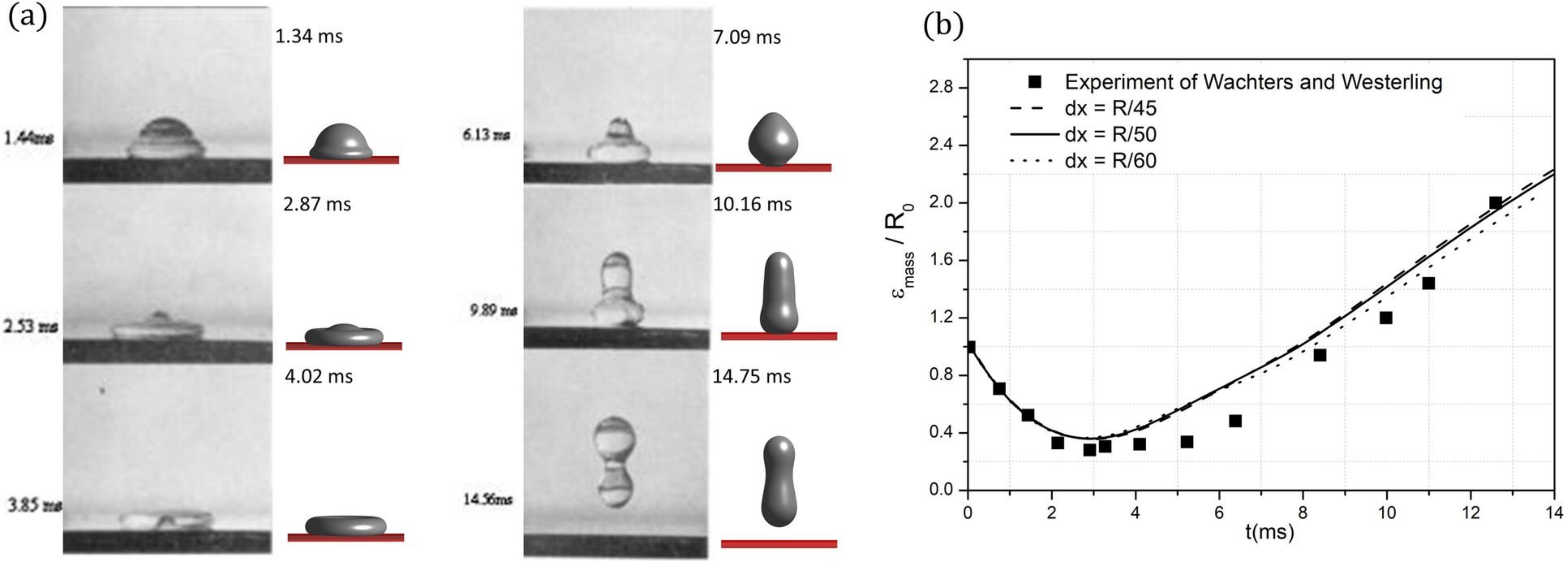
(a)
1.34 ms
1.44ms
2.87 ms
2.53 ms
4.02 ms
3.85 ms
7.09 ms
6.13 ms
10.16 ms
9.89 ms
14.75 ms
14.56ms
(b)
Experiment of Wachters and Westerling
dx = R/45
dx = R/50
dx = R/60
ε_{mass} / R_0
0.0
0.4
0.8
1.2
1.6
2.0
2.4
2.8
0
2
4
6
8
10
12
14
t(ms)

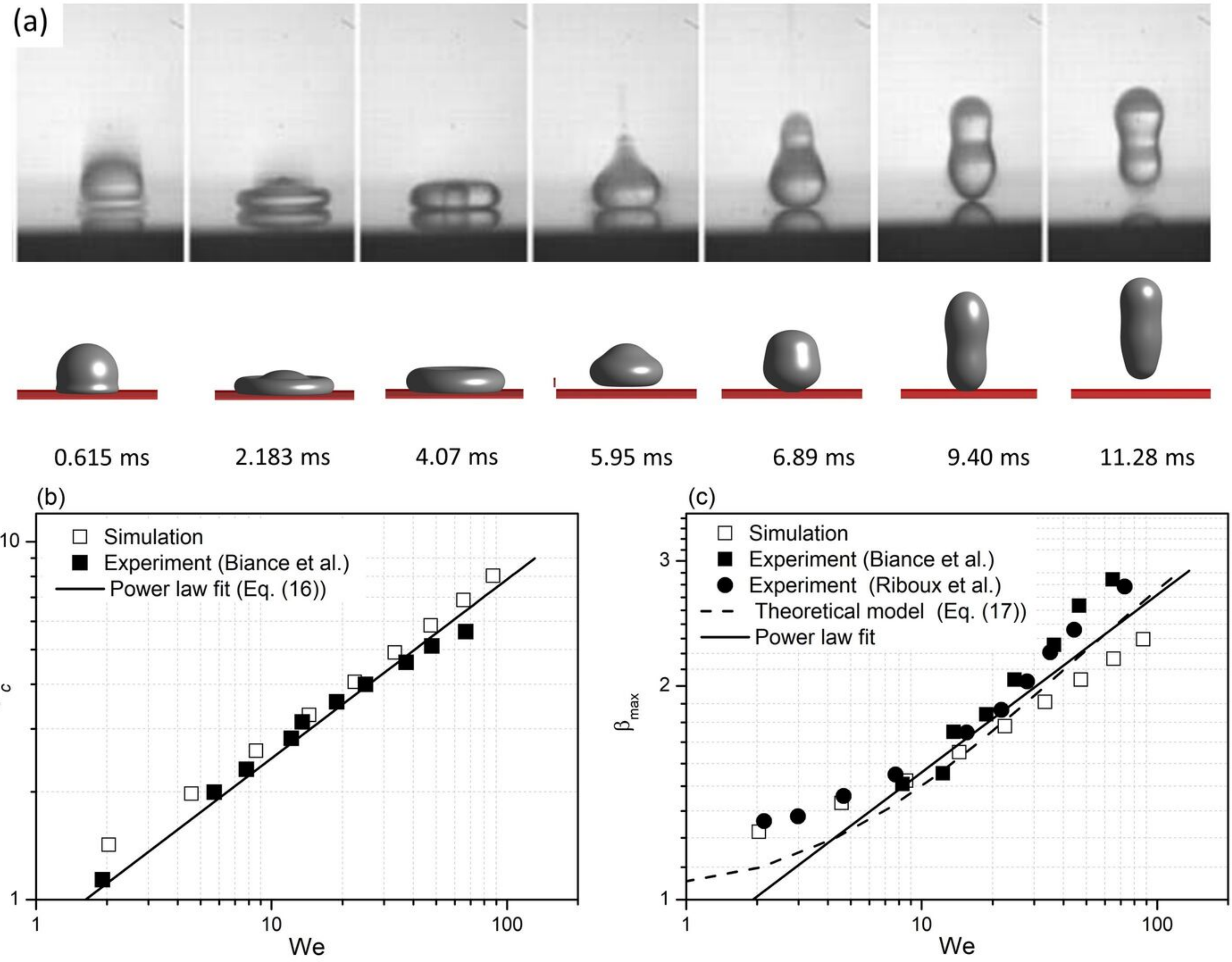
(a)
0.615 ms
2.183 ms
4.07 ms
5.95 ms
6.89 ms
9.40 ms
11.28 ms
(b)
□ Simulation
■ Experiment (Biance et al.)
Power law fit (Eq. (16))
t_c^*
10
1
We
1
10
100
(c)
□ Simulation
■ Experiment (Biance et al.)
● Experiment (Riboux et al.)
Theoretical model (Eq. (17))
Power law fit
β_{max}
3
2
1
We
1
10
100

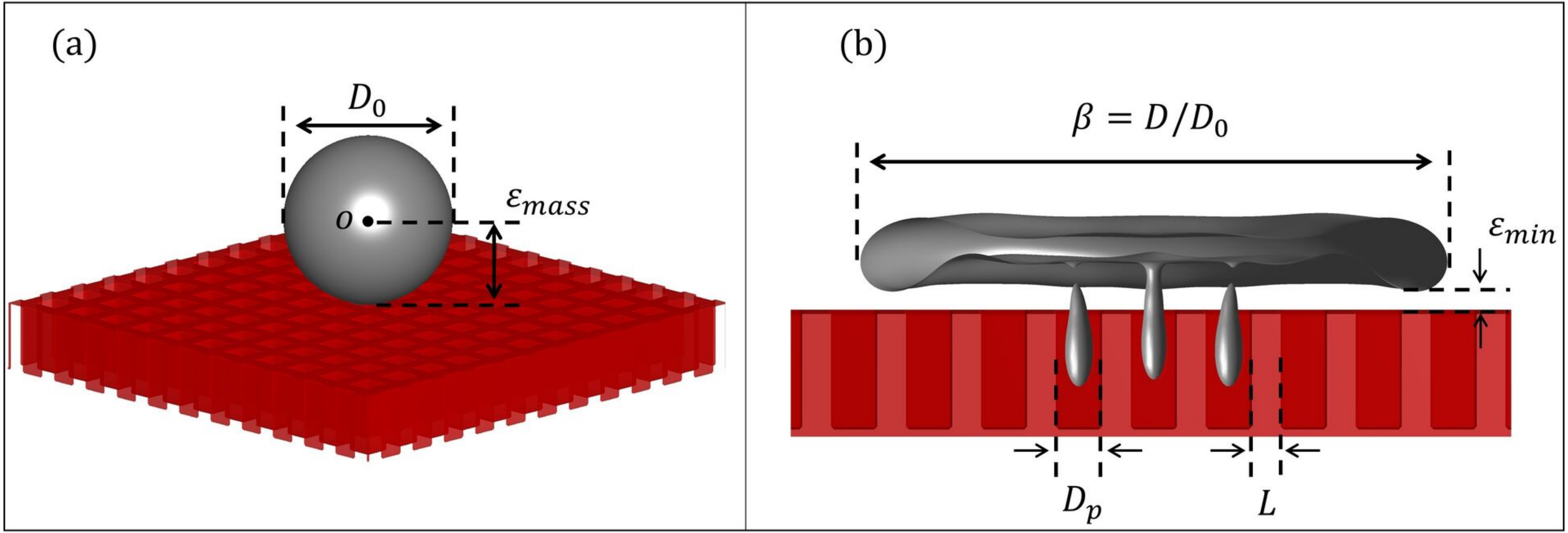
(a)
D_0
o
ε_{mass}
(b)
$\beta = D/D_0$
ε_{min}
D_p
L

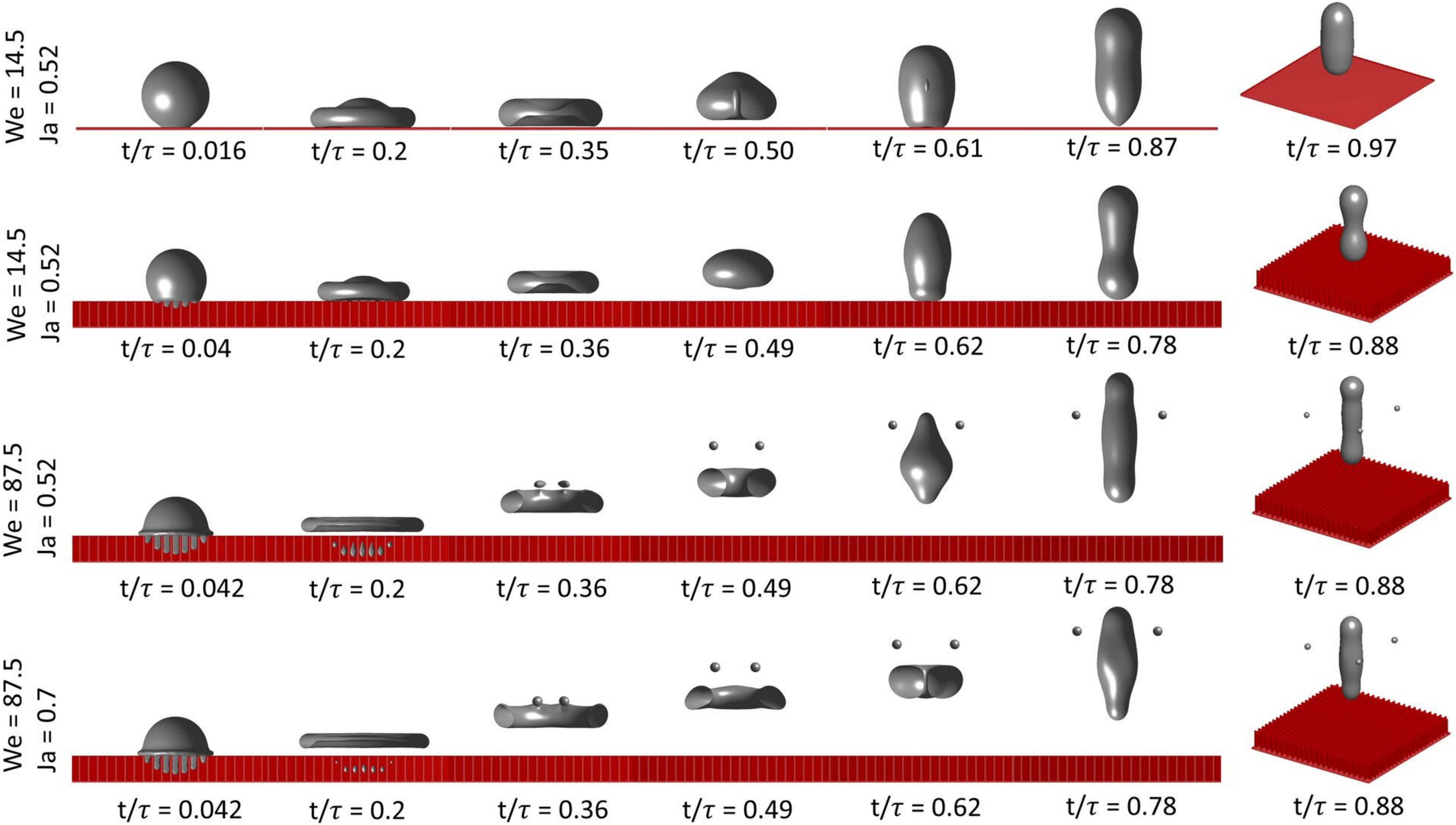
We = 14.5
Ja = 0.52
t/τ = 0.016
t/τ = 0.2
t/τ = 0.35
t/τ = 0.50
t/τ = 0.61
t/τ = 0.87
t/τ = 0.97
We = 14.5
Ja = 0.52
t/τ = 0.04
t/τ = 0.2
t/τ = 0.36
t/τ = 0.49
t/τ = 0.62
t/τ = 0.78
t/τ = 0.88
We = 87.5
Ja = 0.52
t/τ = 0.042
t/τ = 0.2
t/τ = 0.36
t/τ = 0.49
t/τ = 0.62
t/τ = 0.78
t/τ = 0.88
We = 87.5
Ja = 0.7
t/τ = 0.042
t/τ = 0.2
t/τ = 0.36
t/τ = 0.49
t/τ = 0.62
t/τ = 0.78
t/τ = 0.88

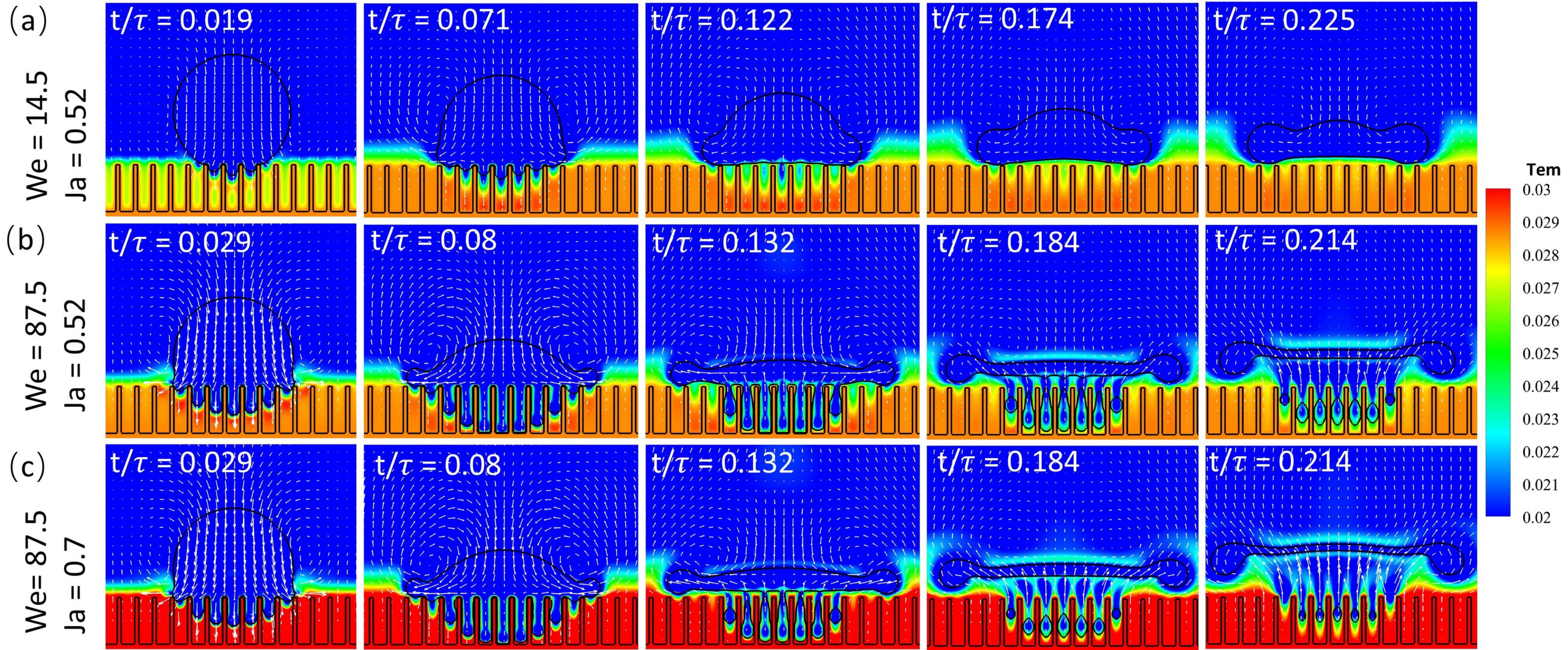
(a)
We = 14.5
Ja = 0.52
t/τ = 0.019
t/τ = 0.071
t/τ = 0.122
t/τ = 0.174
t/τ = 0.225
(b)
We = 87.5
Ja = 0.52
t/τ = 0.029
t/τ = 0.08
t/τ = 0.132
t/τ = 0.184
t/τ = 0.214
(c)
We= 87.5
Ja = 0.7
t/τ = 0.029
t/τ = 0.08
t/τ = 0.132
t/τ = 0.184
t/τ = 0.214
Tem
0.03
0.029
0.028
0.027
0.026
0.025
0.024
0.023
0.022
0.021
0.02

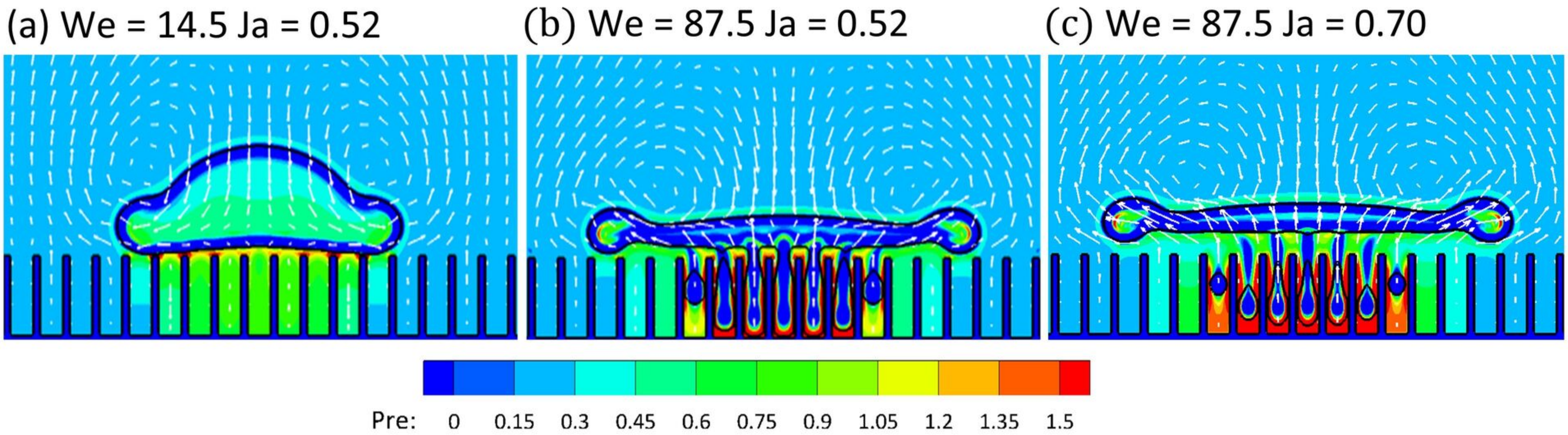
(a) We = 14.5 Ja = 0.52
(b) We = 87.5 Ja = 0.52
(c) We = 87.5 Ja = 0.70
Pre:
0
0.15
0.3
0.45
0.6
0.75
0.9
1.05
1.2
1.35
1.5

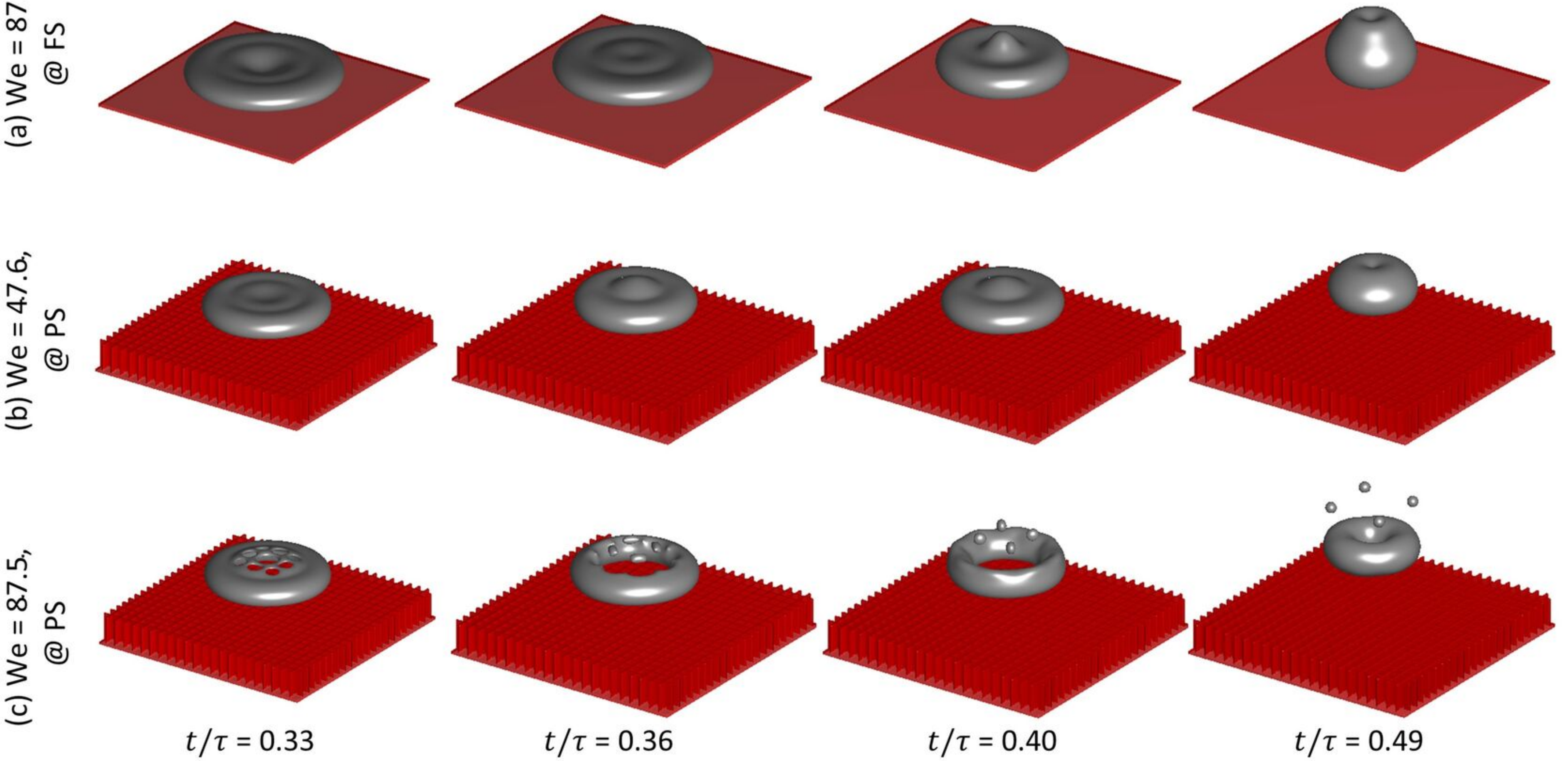
(a) We = 87.5, @ FS
(b) We = 47.6, @ PS
(c) We = 87.5, @ PS
t/τ = 0.33
t/τ = 0.36
t/τ = 0.40
t/τ = 0.49

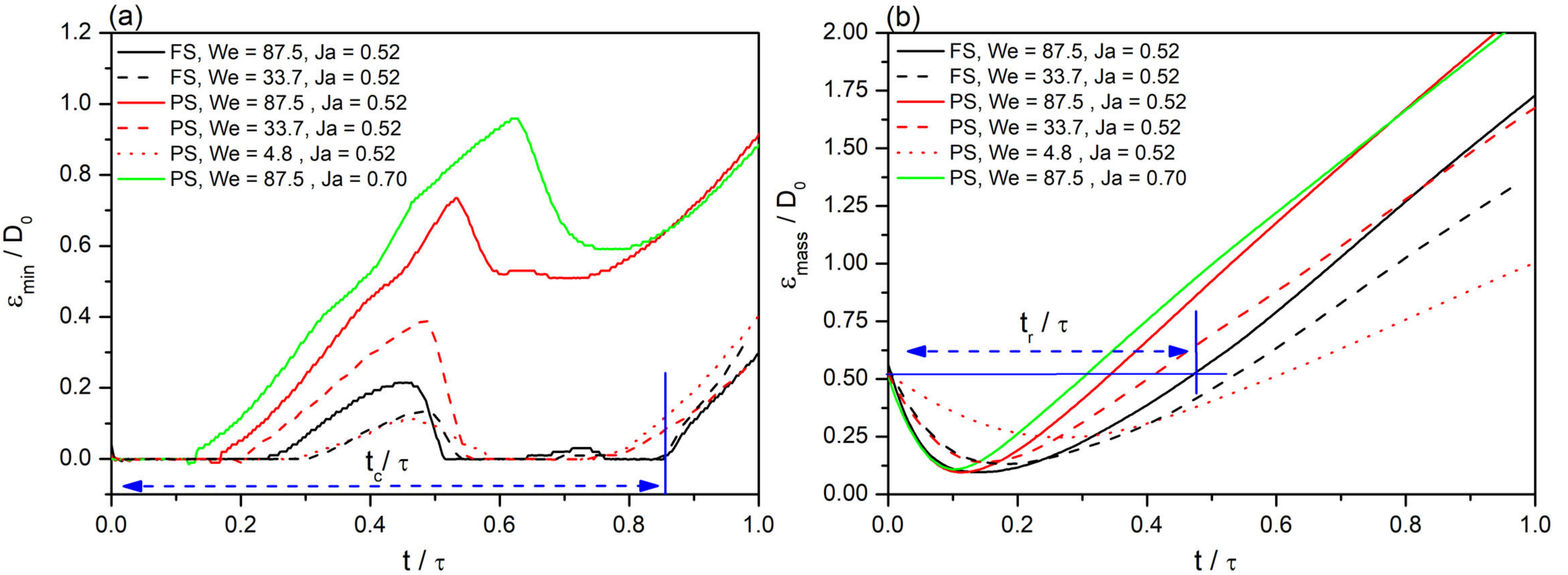
(a)
FS, We = 87.5, Ja = 0.52
FS, We = 33.7, Ja = 0.52
PS, We = 87.5 , Ja = 0.52
PS, We = 33.7, Ja = 0.52
PS, We = 4.8 , Ja = 0.52
PS, We = 87.5 , Ja = 0.70
ε_{min} / D_0
1.2
1.0
0.8
0.6
0.4
0.2
0.0
t_c / τ
0.0
0.2
0.4
0.6
0.8
1.0
t / τ
(b)
FS, We = 87.5, Ja = 0.52
FS, We = 33.7, Ja = 0.52
PS, We = 87.5 , Ja = 0.52
PS, We = 33.7, Ja = 0.52
PS, We = 4.8 , Ja = 0.52
PS, We = 87.5 , Ja = 0.70
ε_{mass} / D_0
2.00
1.75
1.50
1.25
1.00
0.75
0.50
0.25
0.00
t_r / τ
0.0
0.2
0.4
0.6
0.8
1.0
t / τ

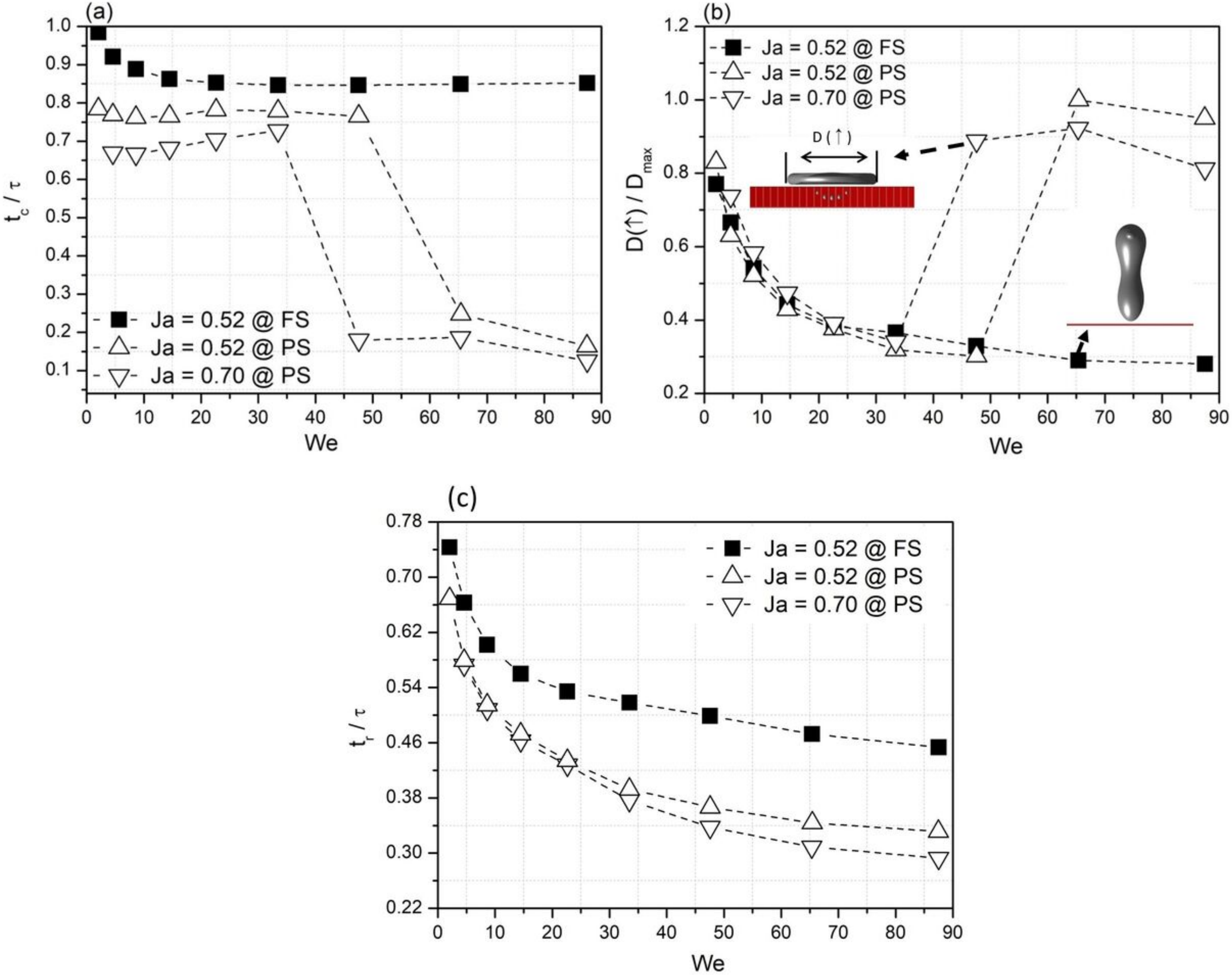
(a)
t_c / τ
1.0
0.9
0.8
0.7
0.6
0.5
0.4
0.3
0.2
0.1
0
10
20
30
40
50
60
70
80
90
We
Ja = 0.52 @ FS
Ja = 0.52 @ PS
Ja = 0.70 @ PS
(b)
$D(\uparrow) / D_{max}$
1.2
1.0
0.8
0.6
0.4
0.2
0
10
20
30
40
50
60
70
80
90
We
Ja = 0.52 @ FS
Ja = 0.52 @ PS
Ja = 0.70 @ PS
D (↑)
(c)
t_r / τ
0.78
0.70
0.62
0.54
0.46
0.38
0.30
0.22
0
10
20
30
40
50
60
70
80
90
We
Ja = 0.52 @ FS
Ja = 0.52 @ PS
Ja = 0.70 @ PS

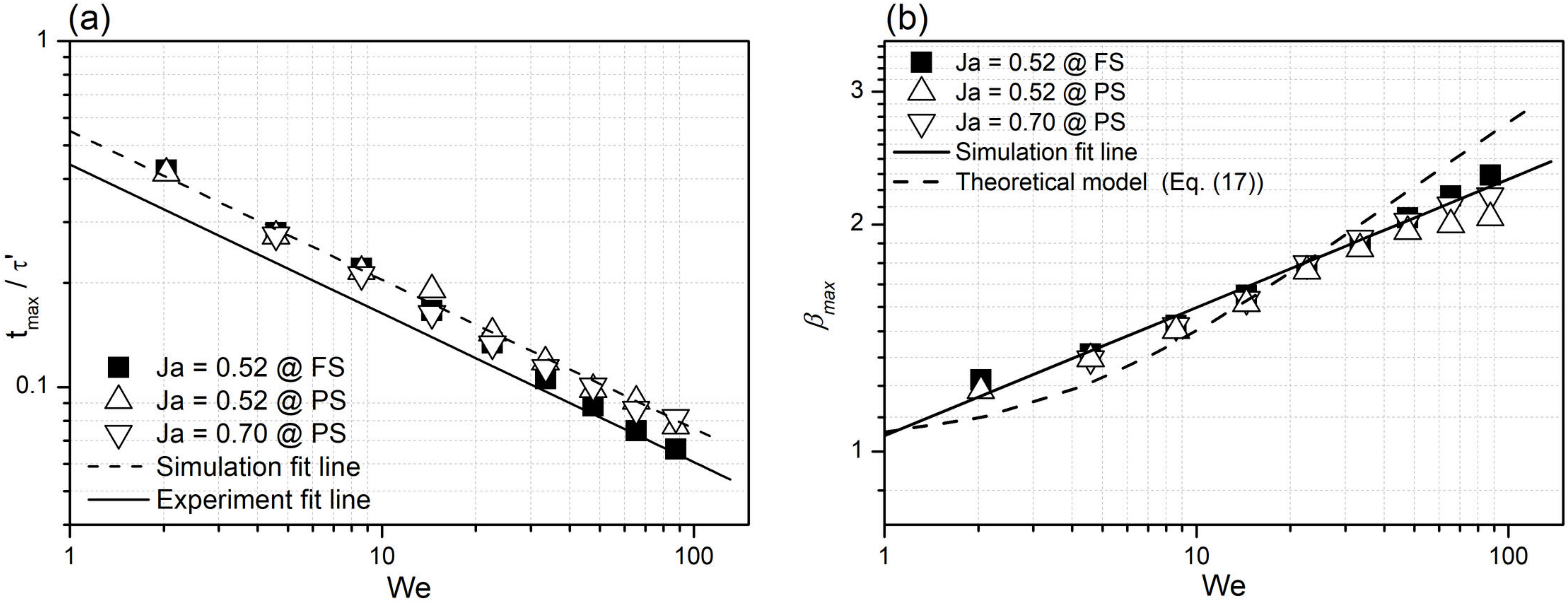
(a)
1
0.1
t_{max} / τ'
1
10
100
We
Ja = 0.52 @ FS
Ja = 0.52 @ PS
Ja = 0.70 @ PS
Simulation fit line
Experiment fit line
(b)
3
2
1
β_{max}
1
10
100
We
Ja = 0.52 @ FS
Ja = 0.52 @ PS
Ja = 0.70 @ PS
Simulation fit line
Theoretical model (Eq. (17))

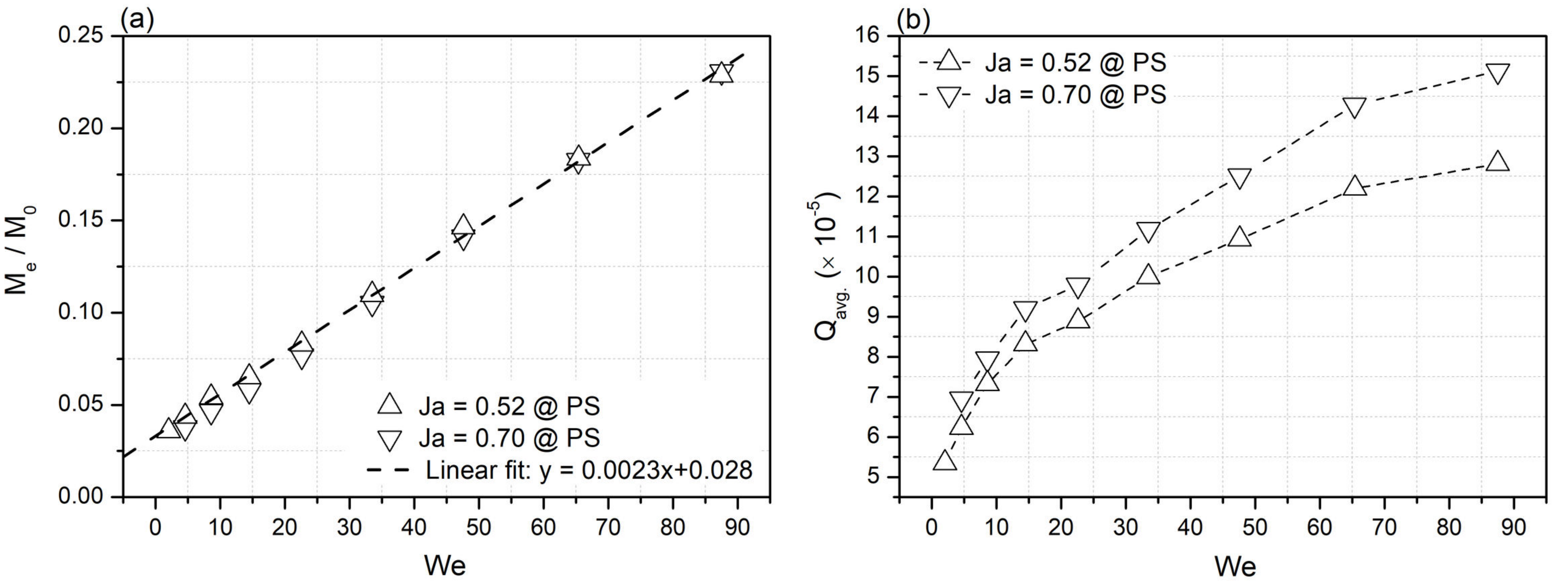
(a)
M_e / M_0
0.25
0.20
0.15
0.10
0.05
0.00
0
10
20
30
40
50
60
70
80
90
We
Ja = 0.52 @ PS
Ja = 0.70 @ PS
Linear fit: y = 0.0023x+0.028
(b)
$Q_{avg.}$ (× 10^{-5})
16
15
14
13
12
11
10
9
8
7
6
5
0
10
20
30
40
50
60
70
80
90
We
Ja = 0.52 @ PS
Ja = 0.70 @ PS

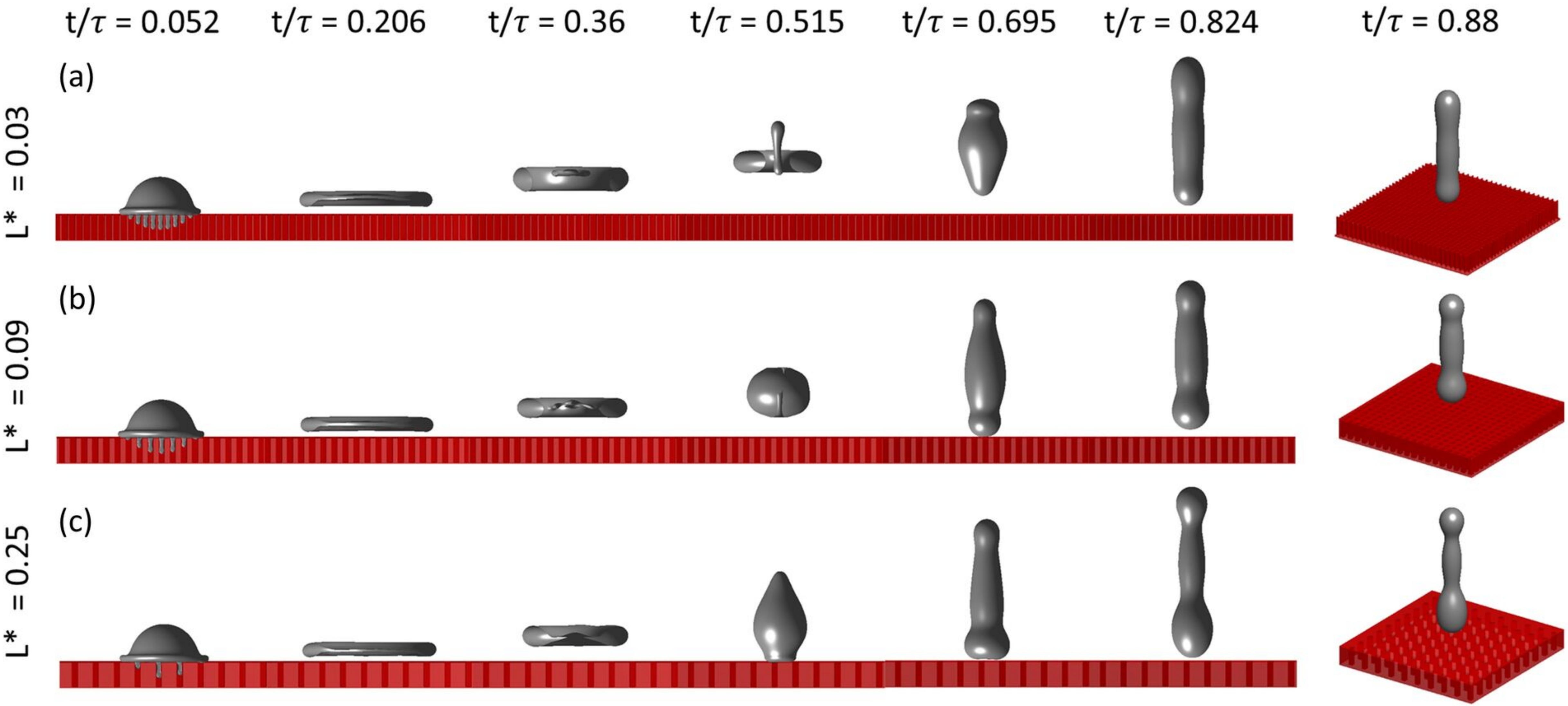
t/τ = 0.052
t/τ = 0.206
t/τ = 0.36
t/τ = 0.515
t/τ = 0.695
t/τ = 0.824
t/τ = 0.88
(a)
L* = 0.03
(b)
L* = 0.09
(c)
L* = 0.25

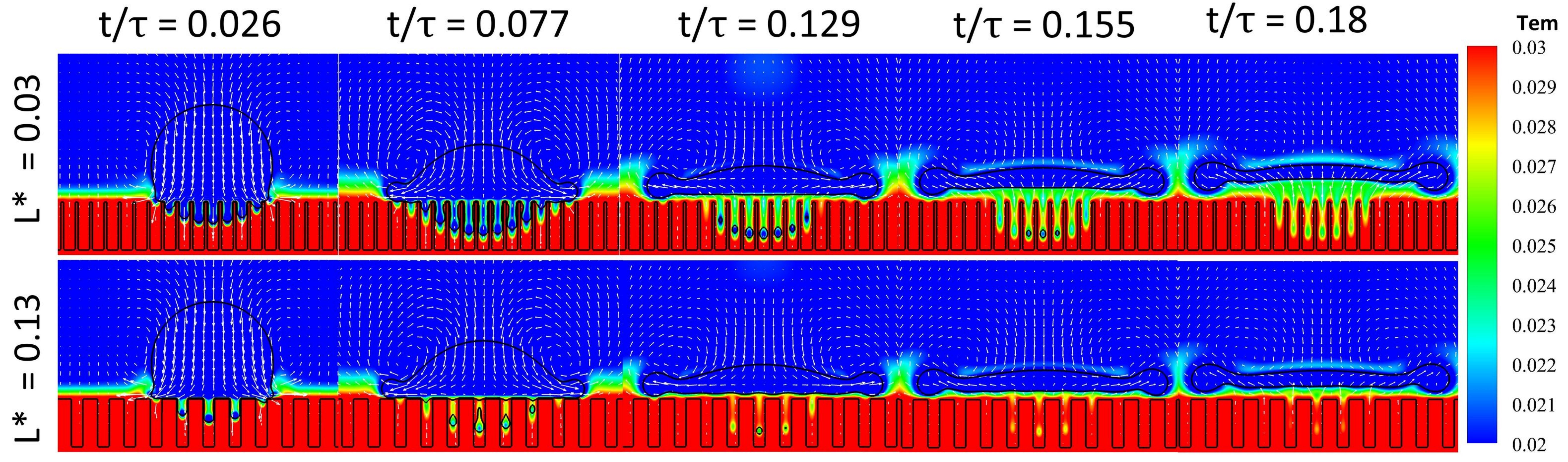
t/τ = 0.026
t/τ = 0.077
t/τ = 0.129
t/τ = 0.155
t/τ = 0.18
L* = 0.03
L* = 0.13
Tem
0.03
0.029
0.028
0.027
0.026
0.025
0.024
0.023
0.022
0.021
0.02

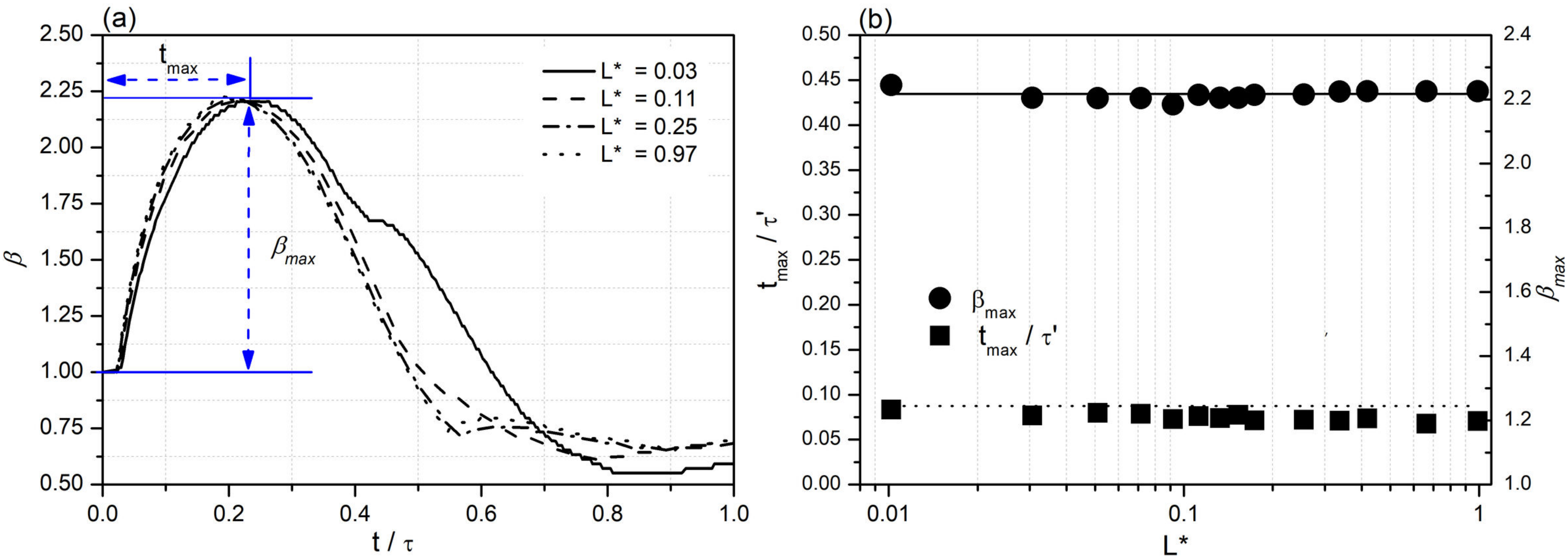
(a)
β
t / τ
t_max
β_max
L* = 0.03
L* = 0.11
L* = 0.25
L* = 0.97
2.50
2.25
2.00
1.75
1.50
1.25
1.00
0.75
0.50
0.0
0.2
0.4
0.6
0.8
1.0
(b)
t_max / τ'
β_max
L*
β_max
t_max / τ'
0.50
0.45
0.40
0.35
0.30
0.25
0.20
0.15
0.10
0.05
0.00
0.01
0.1
1
2.4
2.2
2.0
1.8
1.6
1.4
1.2
1.0

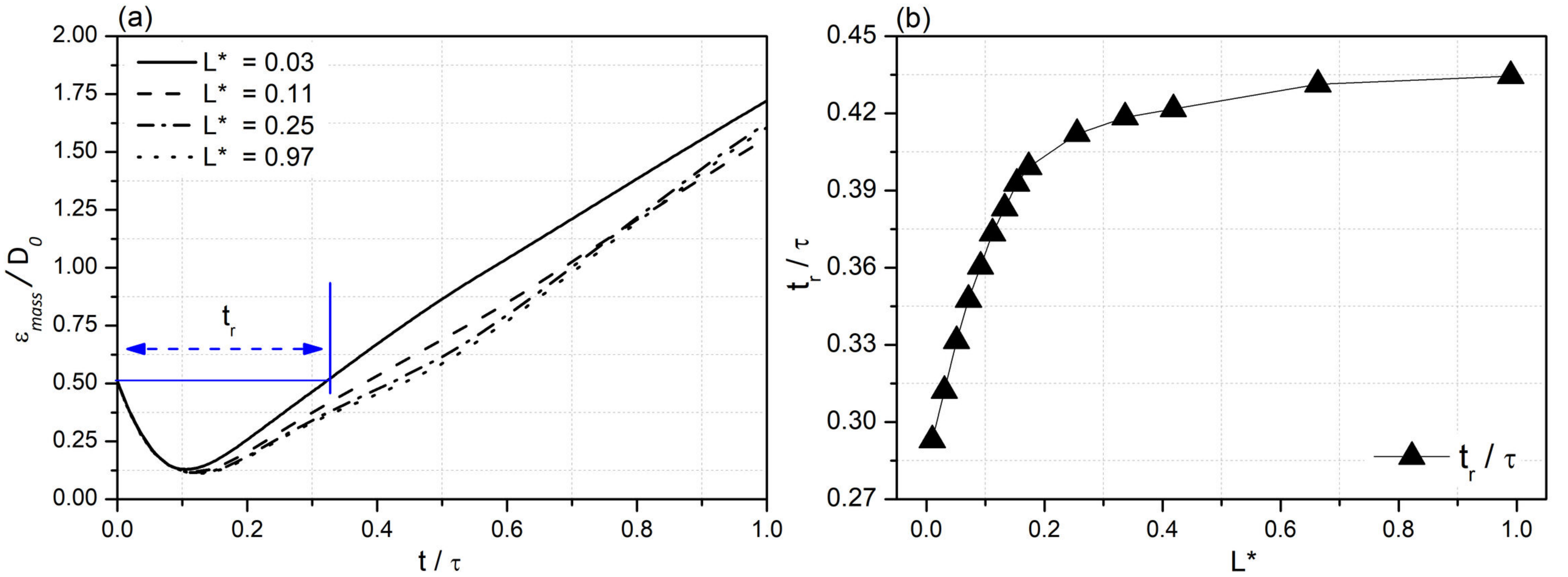
(a)
(b)
ε_{mass} / D_0
t / τ
t_r
L* = 0.03
L* = 0.11
L* = 0.25
L* = 0.97
0.00
0.25
0.50
0.75
1.00
1.25
1.50
1.75
2.00
0.0
0.2
0.4
0.6
0.8
1.0
t_r / τ
L*
0.27
0.30
0.33
0.36
0.39
0.42
0.45
0.0
0.2
0.4
0.6
0.8
1.0

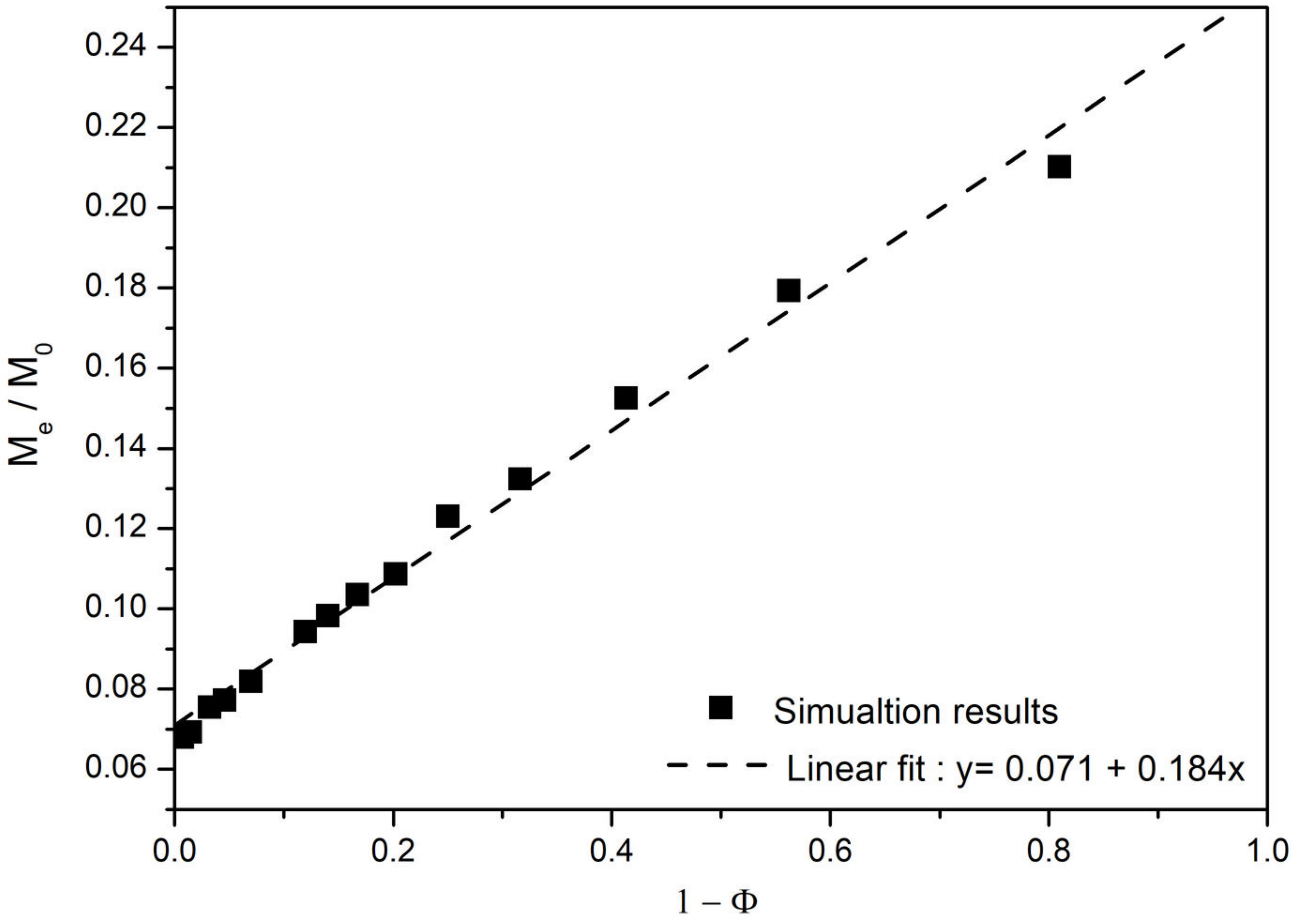
0.24
0.22
0.20
0.18
0.16
0.14
0.12
0.10
0.08
0.06
M_e / M_0
0.0
0.2
0.4
0.6
0.8
1.0
$1 - \Phi$
Simualtion results
Linear fit : y= 0.071 + 0.184x

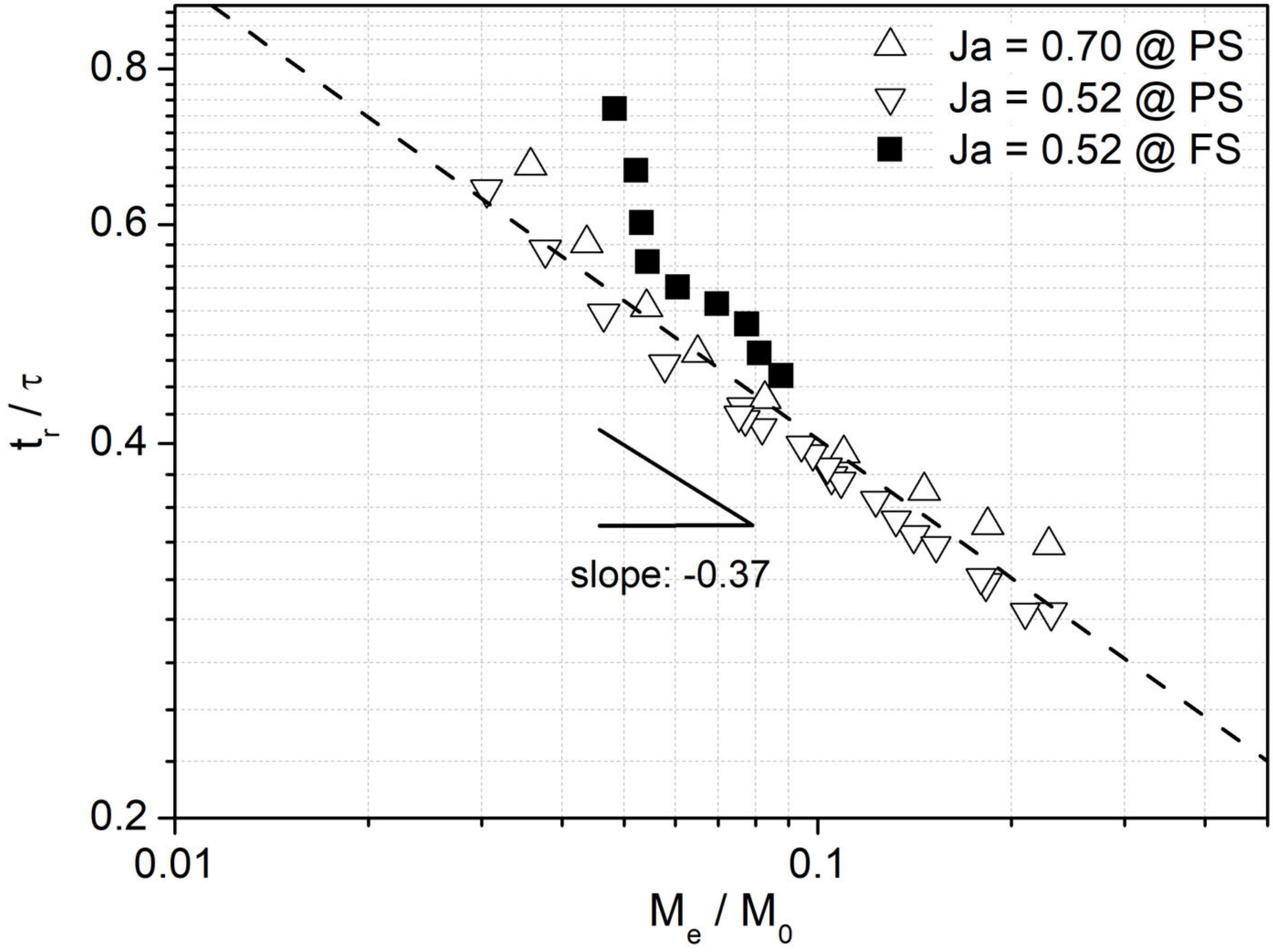

Ja = 0.70 @ PS
Ja = 0.52 @ PS
Ja = 0.52 @ FS
slope: -0.37
t_r / τ
0.8
0.6
0.4
0.2
0.01
0.1
M_e / M_0